FABRICATION AND CHARACTERIZATION OF SURFACE NANOSCALE AXIAL PHOTONICS MICRORESONATORS

Tabassom Hamidfar

A thesis
in
The Department
of
Physics

Presented in Partial Fulfillment of the Requirements
For the Degree of Master of Science (Physics)
Concordia University
Montréal, Québec, Canada

April 2015

Concordia University
School of Graduate Studies

This is to certify that the thesis prepared

By: **Tabassom Hamidfar**

Entitled: **Fabrication and characterization of surface nanoscale axial photonics microresonators**

and submitted in partial fulfillment of the requirements for the degree of

Master of Science (Physics)

complies with the regulations of this University and meets the accepted standards with respect to originality and quality.

Signed by the final examining commitee:

_____ Chair
Dr. Laszlo Kalman

_____ Examiner
Dr. Troung Vo-Van

_____ Examiner
Dr. Sushil Misra

_____ Supervisor
Dr. Pablo Bianucci

Approved _____
Dr. Troung Vo-Van
Chair of department

_____ 2015 _____
Dr. André Roy
Dean of Faculty of Arts and Science

Abstract

Fabrication and characterization of surface nanoscale axial photonics microresonators

Tabassom Hamidfar

Micro-scale, whispering gallery mode (WGM) resonators are important devices for trapping, slowing down, and intensifying light in opto-electronic applications. Of the many available silica-based devices, surface nanoscale axial photonics (SNAP) resonators are a new generation of WGM microresonators, consisting of an optical fiber with nanoscale variations of its effective radius. They have received great attention owing to their advantages over conventional silica-based devices, such as flexibility and ultra-low losses, which lead to ultra-high quality factors. They have demonstrated great potential as photonic micro-devices in switching, slowing light, filtering, lasing, and sensing with high precision, as well as for research on Anderson localization and tunnelling.

In this thesis, we present a new fabrication method for SNAP devices using a regular hydrogen-oxygen torch, requiring less equipment than current techniques. We have characterized our SNAP devices with evanescent spectroscopy, utilizing a tapered optical fiber as an excitation source. The transmission spectroscopy results show that our flame fabricated SNAP devices have modes with very high quality factors ($\sim 10^7$) which can show significant thermal non-linear effects.

Acknowledgments

First and foremost, I would like to express my deepest gratitude to my supervisor, Prof. Pablo Bianucci for his guidance and support throughout the course of this project. His patience, enthusiasm and encouragement fueled my motivation and pushed me farther than I thought I could go.

I would like to thank Prof. Alexandre Champagne and Prof. Laszlo Kalman of Concordia University, for their kind support during my studies at Concordia University. I am extremely grateful to my committee members, Prof. Troung Vo-Van and Prof. Sushil Misra, for their assistance and time.

Many thanks to Marie-Anne Cheong Youne for her kindness and assistance with departmental matters. I am also grateful to Aldo Dissegna for his technical support and assistance in the experimental work.

I would like to thank all my fellow graduate students and postdocs for making my experience at Concordia pleasant and cheerful. Sincere thanks to Kathleen McGarvey Lechable, Amir Hassanpour, Serap Yiğen, Golia Shafiei, Simeon Hanks, and all my colleagues.

My special thanks to my husband and best friend, Amir for his endless love and encouragement. His valuable suggestions and priceless support have been very important to me. I am thankful to my parents and my lovely brother for supporting me all times.

I would like to the gratefully acknowledge the financial support of the Concordia University through the Richard K. Dimond Memorial Fund and the Faculty of Arts and Science graduate fellowship. Financial support during my studies was provided in part by NSERC and FQRNT.

Contents

List of Figures

List of Tables

Chapter 1

Introduction

1.1 Introduction

In the last decade, an important goal in the research and development of opto-electronic devices has been to build micro-scale devices for trapping and slowing light. Silica-based whispering gallery modes (WGM) resonators have proven popular due to their low losses, very high quality factors, and ease of fabrication. Surface Nanoscale Axial Photonics (SNAP) devices are a new generation of WGM microresonators, which consist of an optical fiber with nanoscale variations of its effective radius.

The idea of producing SNAP devices was first published by M. Sumetsky and J. M. Fini in 2011[1, 2]. They have demonstrated two methods of fabrication based on the modification of the effective radius for a variety of glass and photosensitive fibers with IR (CO_2 laser) [3] and UV beam exposures [4]. SNAPs devices with more complex shapes, including bottle resonators with parabolic and semi-parabolic variations, have

also been developed recently [5].

1.2 Contributions

In this thesis, we introduced a new fabrication method for SNAP devices that uses a regular hydrogen-oxygen torch. Current methods require equipment that might not be easily available, such as carbon dioxide lasers. Such equipment is not required for our fabrication technique.

We have implemented a flame brushing technique and we have successfully fabricated tapered fibers with diameters of $1 - 2\ \mu m$ with our own recipe, which generate a strong evanescent field. We have presented recipes to fabricate SNAP device with diameters in the range of $20 - 95\ \mu m$.

We have characterized our SNAP devices with evanescent spectroscopy, where the excitation source is a tapered optical fiber. We designed and built a precise set-up to have maximum control on the positions of the SNAP device and the tapered fiber for characterization of our SNAP devices. The transmission spectroscopy results show that our flame-fabricated SNAP devices have the potential to host very high quality factors up to the order of 10^7, with some resonances demonstrating significant thermal nonlinear effects.

1.3 Thesis outline

The present research work is directed towards the introduction of a new low cost fabrication method to make SNAP devices. The thesis comprises 5 chapters. Chapter 1 (the present chapter) provides a general introduction, contributions and the thesis outline.

In chapter 2, we briefly review the theoretical background of SNAP device and SNAP theory, including an analogy to quantum mechanics concerning the behaviour of light at the surface of an optical fiber.

In chapter 3, we explain common fabrication methods for micro-fibers, nano-fibers, and SNAP devices. We then describe the fabrication technique that we used to make a tapered fiber. Our new, low cost method to fabricate a SNAP device is introduced. In chapter 4, we first describe the measurement set-up used for the characterization of the SNAP devices, followed by a presentation of our spectroscopy results. In chapter 5, we present the main conclusions and suggestions for future research.

Chapter 2

Theoretical Background

In this chapter, a theoretical background of surface nanoscale axial photonics is presented before introducing our experimental work in chapter 3. First, a brief overview of optical fibers and some commonly used concepts is given. We then introduce the SNAP device and SNAP theory, including an analogy describing the "quantum mechanics" of light at the surface of a SNAP device.

2.1 Optical Fiber

Since the 1970s, optical glass fibers have been widely used for different applications, including the low-loss transmission of optical signals in telecommunications [6], medication [7], and nonlinear optics [8]. They also have been utilized as astronomical instruments[12], sensors [9], filters [10], and lasers [11]. An optical fiber is a transparent and flexible line of ultra pure glass with a diameter of approximately

the size of a human hair. A single optical fiber consist of three layers: (i) a cylindrical core, with a high refractive index, n_1, (ii) a cladding, with a lower refractive index, n_2 and (iii) an outer protection polymer buffer (see Fig. 2.1).

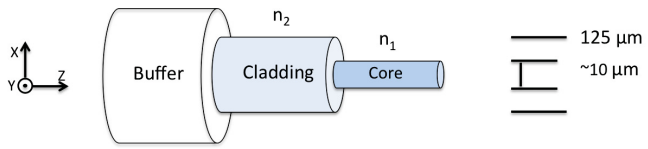

Figure 2.1: A standard optical fiber.

Optical fibers have diverse applications. The dimensions of an optical fiber depend on its application. For example, fiber optics sensors use fibers with a diameter of the order of tens of micrometers with various different core diameters. For laser power delivery, the fiber diameter is larger than 1 mm with a core diameter of 100 μm [13]. In the case of a standard, single mode fiber used for optical communications, the fiber diameter is 125 μm and the core diameter is about 10 μm.

Glass fiber is usually made by a drawing process that uses a drawing tower. A large diameter preform is melted, drawn, and collected by a tractor mechanism [14]. Therefore the diameter of the fiber is controllably reduced.

An optical fiber can be considered as a cylindrical waveguide based on light guiding via total internal reflection in dielectric structures. To better understand total internal reflection, Snell's law must first be explained. Snell's law describes the behaviour of light or other types of waves at a dielectric interface. Snell's law of refraction and reflection of light is shown in Figure 2.2.

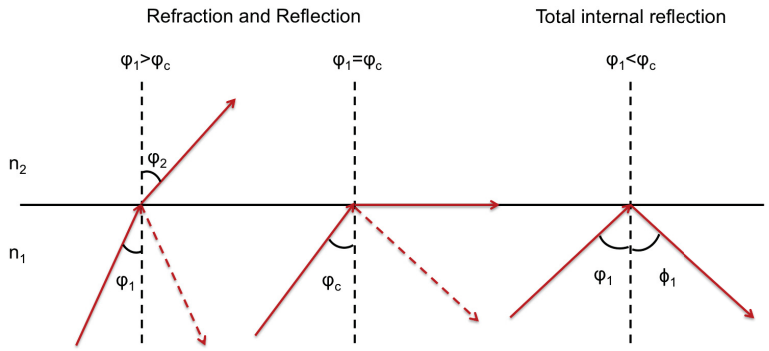

Figure 2.2: Snell's law of refraction, reflection and total internal reflection.

According to Snell's law, the ratio of the sines of the angles of refraction and incidence is equivalent to the ratio of the indices of refraction

$$\sin(\varphi_1)/\sin(\varphi_2) = n_2/n_1 \tag{2.1}$$

where n_1 and n_2 are the refractive indices of the two dielectric materials and φ_1 and φ_2 are defined as the refracted and incident angles of an electromagnetic wave, respectively.

For total reflection at a dielectric interface (core/cladding) with refractive indices $n_1 > n_2$, a critical angle φ_c is defined when the angle of refraction is equal to 90^o.

$$\sin(\varphi_c) = n_2/n_1 < 1; \varphi_c = \arcsin(n_2/n_1) \sim (\frac{\Delta n}{n_1}) \tag{2.2}$$

where

$$\Delta = \frac{n_1 - n_2}{n_1} \tag{2.3}$$

Here, Δ represents the refractive index difference between the core and cladding materials and is called the normalized index difference.

When a wave's angle of incidence is smaller than the critical angle, we have reflection and refraction of light beams. Alternatively, when the incident angle is larger than φ_c, a total reflection happens.

Figure 2.3 shows schematically the cross section of an optical fiber and how light propagates inside the fiber when the core diameter d is much larger than the optical wavelength λ. Light propagation in a fiber can be modelled as the propagation and reflection of light beams at the dielectric interface formed by the fiber's core, n_1, and cladding, n_2 (where $n_1 > n_2$).

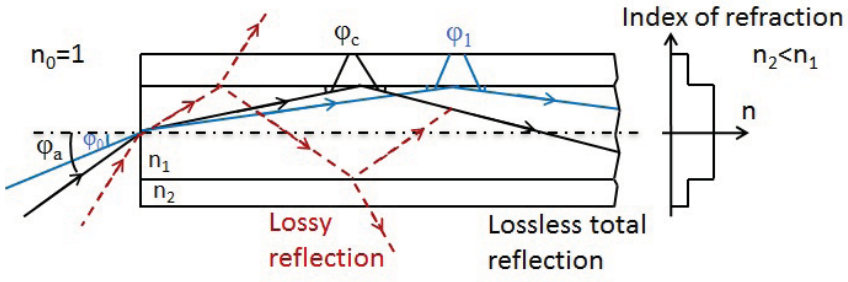

Figure 2.3: A longitudinal section of an optical fiber.

For incoming beams with an entrance angle of φ_0 at the entrance interface of the optical fiber, Snell's law allows us to write

$$n_0 \sin(\varphi_a) = n_1 \sin(\varphi_c) \tag{2.4}$$

In a straight fiber, all rays with an entrance angle smaller than the acceptance angle undergo lossless propagation via total internal reflection, while rays with a larger entrance angle are refracted into the cladding and are diminished by refraction losses.

2.1.1 Modes

The distribution of the field in space is called a mode. Waves which enter an optical fiber with different angles traverse different paths (modes). In an optical fiber, waves with the same mode can have different frequencies. In this kind of fiber, the waves are identically distributed in space, having the same path and giving us a single ray of light. By solving Maxwell's equations, the Helmholtz equation for waves can be obtained. Modes are defined as the possible solutions of the Helmholtz equation.

In general, there are two types of modes in an optical fiber. The first group consists of radiation modes, which transfer energy into the cladding. Radiation modes have a Poynting vector which has a radial component, resulting in losses of the energy in the fiber. Guided modes are the second type of modes that confine the propagation of the field and its energy inside the waveguide's core. In an optical fiber behaving as a cylindrical dielectric waveguide, this type of mode can be further classified into four categories depending on specific field characteristics: (i) transverse electric field

(TE): The magnetic field is oriented along the direction of propagation ($\overrightarrow{H} = H_z\hat{Z}$), (ii) transverse magnetic field (TM): The electric field is oriented along the direction of propagation ($\overrightarrow{E} = E_z\hat{Z}$), (iii) transverse electromagnetic (TEM): There are no field components along the propagation direction ($E_z = H_z = 0$). These modes appear in weakly confining waveguides with a small Δ, and (iv) hybrid mode: Both the electric and magnetic fields are oriented along the direction of propagation ($E_z \neq 0, \quad H_z \neq 0$) in the fiber. Hybrid modes are either HE or EH modes. In EH modes, the axial electric field E_z dominates, while in HE modes the axial magnetic field H_z prevails [15].

Depending on the size of the core and the refractive index contrast, we can have many of these guided modes at the same time. The field inside of a waveguide can be a combination of these modes.

2.1.2 Single-mode and Multi-mode fiber

Single-mode fibers are a kind of optical fiber which have a core diameter slightly larger than the wavelength of light, typically between 8 to 12 μm for near infrared light. In contrast, optical fibers with a core diameter much larger than the wavelength of light, between 50 to 100 μm, are known as multi-mode fibers. These fibers also have multi-transverse modes and thus have a high modal dispersion (which is explained in the next subsection). The cladding diameter of 125 μm is the standard number for both single-mode and multi-mode fibers (see Figure 2.4).

Waves with different modes inside of an optical fiber have different propagation

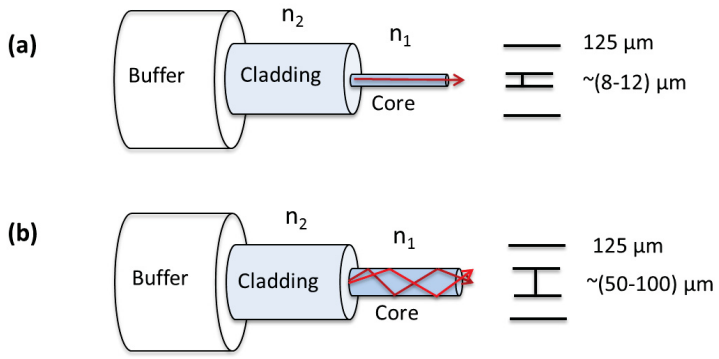

Figure 2.4: **a.** A single-mode(SM) optical fiber. **b.** A multi-mode(MM) optical fiber. They differ only in the diameter of the guiding core.

velocities and patterns to pass along the fiber, and correspondingly have different transit times to traverse the length of the fiber. As a result, a distribution of arrival times is defined as *modal dispersion*. Modal dispersion is considered as a problem in different optical fiber applications[17].

Although multi-mode fibers have higher in-coupling efficiency and show fewer losses when connected together, they are only preferable when used for short distances and when the highest data transmission rate is not required. On the other side, single-mode fibers are widely used in communication systems due to their higher data transmission rates over long distances and their very low modal dispersion. [18].

2.1.2.1 Numerical aperture

The numerical aperture (NA) for fiber characterization is defined as

$$NA = \sin(\varphi_a) = \frac{1}{n_0}\sqrt{n_1^2 - n_2^2} \tag{2.5}$$

For weakly guiding fibers with small $\Delta n = n_1 - n_2 \sim 0.01$, we can write

$$NA = \frac{n_1}{n_0}\sqrt{1 - (\frac{n_2}{n_1})^2} \approx \frac{n_1}{n_0}\sqrt{2(1 - \frac{n_2}{n_1})} \approx \frac{n_1}{n_0}\sqrt{2\Delta} \tag{2.6}$$

In general, Δ is about $0.2 - 1$ % for a single mode fiber (SM) and around $1 - 3$ % for a multimode fiber (MM). A small numerical aperture means it is more challenging to couple light into a fiber's core and also gives a small Δ. On the other hand, modal dispersion from total internal propagation becomes low [18]. Large index differences between the core and cladding leads to a large numerical aperture, entrance angle and critical angle, resulting in a high coupling efficiency between an optical fiber and external light sources. In single mode fibers, the numerical aperture is about 0.1, while multimode fibers have higher NAs ($\sim 0.2 - 0.3$). It is worth mentioning that time delays or modal dispersion are also large for multimode fibers [19].

2.1.3 Whispering gallery modes (WGM)

In closed convex structures with a higher refractive index than the surrounding medium, we find waves known as whispering gallery modes (WGMs). Inside the convex structure, total internal reflection traps light. A ray of light launched inside at grazing incidence will be reflected at the boundary and eventually returns to its initial position (see Figure 2.5). Only certain wavelengths will interfere constructively and build up the modal field. These wavelengths are known as *resonances*. Figure 2.6 shows whispering gallery modes in four different device geometries.

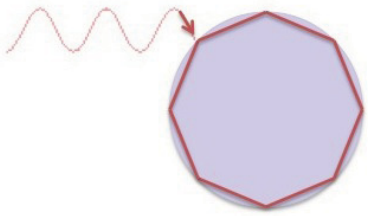

Figure 2.5: Whispering Gallery Mode (WGM) propagation inside a cavity.

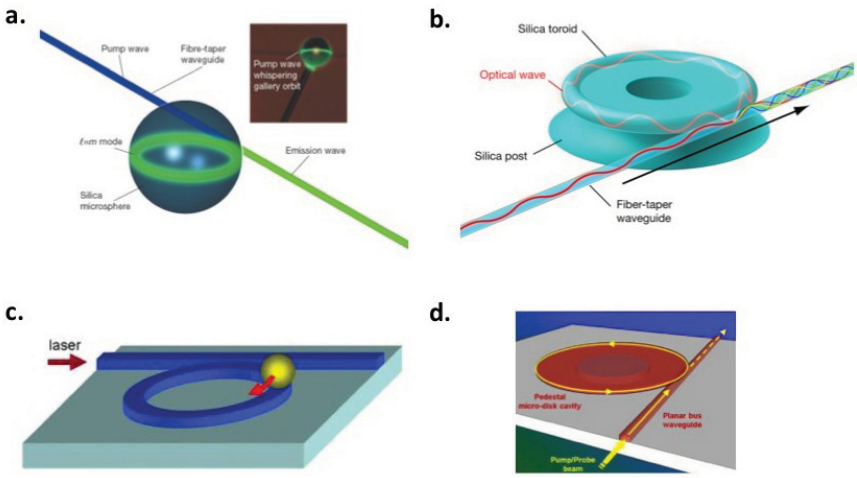

Figure 2.6: Different types of WGM resonators, **a.** Silica microsphere whispering gallery resonators [20]. **b.** Microtoroid resonators [21]. **c.** Microring resonators [22]. **d.** Microdisk resonators [23].

2.1.4 Quality factor

Generally, the quality factor is a dimensionless parameter related to loss of energy in an oscillatory system. It is defined as the resonance wavelength over the full width half maximum (FWHM) of the mode (see Figure 2.7). In an optical resonant structure, the Q-factor is proportional to the decay time of the mode, which in turn

is inversely related to the loss mechanisms, such as surface scattering and absorption in the medium.

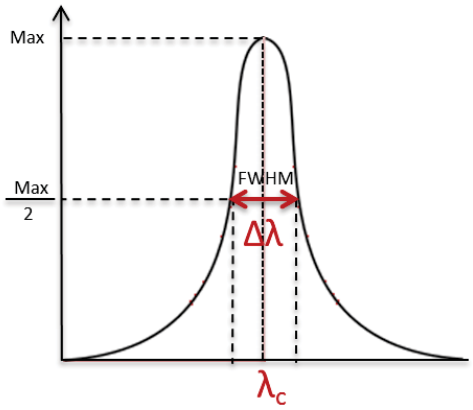

Figure 2.7: Definition of Quality factor of mode.

$$Q = \frac{Resonance\ wavelength \quad (\lambda_c)}{Full\ width\ half\ maximum\ of\ mode \quad (\Delta\lambda)} \tag{2.7}$$

A high quality factor means that the rate of energy loss is lower and that the magnitude of the field inside is stronger.

2.1.5 Maxwell's equations

For a theoretical description of how an electromagnetic wave propagates through an optical fiber, we have to look at Maxwell's equations. Maxwell's equations are defined as

$$\nabla \times \vec{E} = -\frac{\partial \vec{B}}{\partial t}, \quad \nabla \times \vec{H} = \vec{J} + \frac{\partial \vec{D}}{\partial t} \tag{2.8}$$

$$\nabla.\overrightarrow{D} = \rho, \;\; \nabla.\overrightarrow{B} = 0 \tag{2.9}$$

where $\vec{E}$ and $\vec{H}$ are the electric and magnetic fields (V/m and A/m), $\vec{J}$ and ρ are the current and charge densities (A/m^2 and As/m^3), $\vec{D}$ is the dielectric displacement (As/m^2) and $\vec{B}$ is the magnetic induction (Vs/m^2 or T). Because we need these equations to describe the field inside a medium, we have to consider the constitutive relations of the materials. Therefore, we must also consider the following equations:

$$\vec{D} = \epsilon_0 \vec{E} + \vec{P} \tag{2.10}$$

$$\vec{B} = \mu_0(\vec{H} + \vec{M}), \tag{2.11}$$

where ϵ_0 and μ_0 are the dielectric constant and permeability constant of vacuum. In a linear, isotropic, and homogeneous dielectric waveguide, the polarization depends linearly on the electric field.

$$\vec{P} = \epsilon_0 \chi \vec{E} \tag{2.12}$$

where χ is called the electric susceptibility of the material. Thus, we can rewrite Equation 2.10 as

$$\vec{D} = \epsilon_0 \vec{E} + \epsilon_0 \chi \vec{E} = \epsilon_0 (1 + \chi) \vec{E} = \epsilon \vec{E} \tag{2.13}$$

Here, ϵ is the electric permittivity of dielectric constant of the materials ($\epsilon = \epsilon_r \epsilon_0$). In the situation consisting only of dielectric materials, such as glass and air, we can use the following assumptions: (i) charge-free insulator $\rho = 0$; (ii) no currents $\vec{J} = 0$; and (iii) no magnetization $\vec{M} = 0$. As a result, we can simplify Maxwell's equations to [24]

$$\nabla \times \overrightarrow{E} = -\mu \frac{\partial}{\partial t} \overrightarrow{H}, \tag{2.14}$$

$$\nabla \times \overrightarrow{H} = \epsilon \frac{\partial}{\partial t} \overrightarrow{E}, \tag{2.15}$$

$$\nabla . \overrightarrow{E} = 0, \;\; \nabla . \overrightarrow{H} = 0 \tag{2.16}$$

where μ is the magnetic permeability ($\mu = \mu_r \mu_0$) and considering only dielectric materials which are non-magnetic $\mu = \mu_0$.

Taking the curl of the equation 2.14, we can write

$$\nabla \times \nabla \times \overrightarrow{E} = -\mu \frac{\partial}{\partial t} (\nabla \times \overrightarrow{H}) \tag{2.17}$$

By using Equation 2.15, we have

$$\nabla^2 \overrightarrow{E} = -\mu\epsilon \frac{\partial^2}{\partial t^2} \overrightarrow{E} \tag{2.18}$$

Finally, assuming a harmonic time dependence ,$\exp^{+i\omega t}$, for the field, the Helmholtz equation can be derived

$$(\nabla^2 + k^2)\psi = 0 \ , \ \psi = \vec{E}, \vec{H} \tag{2.19}$$

where $k^2 = \mu\epsilon\omega^2$. Considering that $\omega = \frac{kc}{n}$, we can write

$$\mu\epsilon = \frac{n^2}{c^2} \tag{2.20}$$

where n is the refractive index of the material.

2.2 Surface Nanoscale Axial Photonics (SNAP)

Surface Nanoscale Axial Photonics (SNAPs) devices, a new generation of silica-based whispering gallery modes (WGMs) resonators with properties of low losses and high quality factors, consist of an optical fiber with variation of its radius and refractive index [25]. The variation of radius is on the order of a few nanometers (see Fig. 2.8) The radius of a fiber, r_0, is a few tens of μm and $\Delta r(z)$ is a few nm. Variation of the fiber radius is $\Delta r(z) = r(z) - r_0$ and the refractive index is defined as $\Delta n_f(z) = n_f(z) - n_{f0}$. The effective optical radius is given by

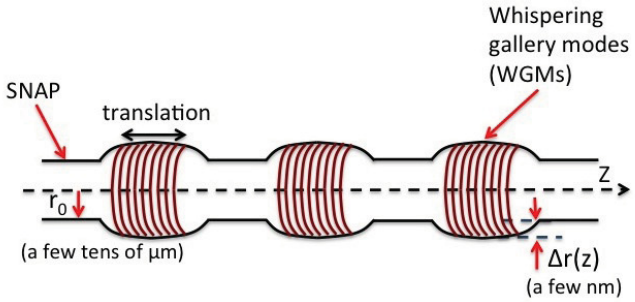

Figure 2.8: Schematic of a Surface Nanoscale Axial Photonic (SNAP) device.

$$r_{eff}(z) = n_f r(z) \tag{2.21}$$

and the effective radius variation can be given as

$$\Delta r_{eff}(z) = r_0 \Delta n_f(z) + n_{f0} \Delta r(z) \tag{2.22}$$

In standard optical fibers, light with a wavelength of λ is guided along the fiber's core. The propagation constant of the light is defined as $\beta_0(\lambda) = \frac{2\pi n_{f0}}{\lambda}$ and the speed of light is $v_0 = \frac{c}{n_{f0}}$. In a SNAP device, light based on whispering gallery modes travels around the surface of the optical fiber and slowly propagates along the fiber axis. Because of the propagation of the light in this direction, the propagation constant of the modes along the z-axis becomes low ($\beta << \beta_0(\lambda)$) and the axial speed of the modes is slower than the speed of light in regular fibers (i.e. $v << v_0$) [26]. In addition, the propagation of the light is restricted to the region of the fiber containing the radius variation and light can not escape.

SNAP devices are particularly interesting because of their low optical losses. They are made of silica, which has low absorption and a smooth surface that reduces the scattering of light.

Table 2.1 summarizes the properties of SNAP devices as compared to prior photonic devices. The advantages of a SNAP device include attributes such as robust whispering gallery modes which are localized inside of the fiber and properties of silica such as roughness of the surface and low material losses. Moreover, because of the micrometer dimensions and low attenuation coefficients of SNAP, these photonic devices can be considered as a suitable platform for miniature integrated photonic circuits.

Table 2.1: SNAP vs. previously developed photonic technologies [27]

Platform	Illustration	Dimension of elements	Propagation loss	Fabrication accuracy
Planar high index contrast	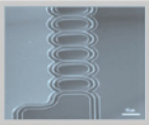	10 µm	0.1 dB/cm	10 nm
Planar low index contrast	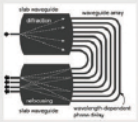	1000 µm	0.01 dB/cm	10 nm
Photonic crystals	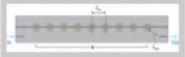	1 µm	0.01 dB/cm	10 nm
Silica micro resonators	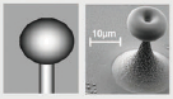	10 µm	0.0001 dB/cm	100 nm
Surface nanoscale axial photonics		10 µm	0.0001 dB/cm	0.1 nm

The characteristic dimensions of individual SNAP elements can potentially be as small as $10\mu m$. While dimensions of this scale are equal to or greater than the dimensions of previous devices, such as silica micro resonators or photonic crystals, the propagation loss of SNAP devices can be up to two orders of magnitude smaller than that of those devices. Also, the fabrication accuracy of SNAP devices can be significantly better than previous technologies.

2.2.1 Coupling light

In general, coupling describes the energy transfer process from one medium to another. In optics, when two or more optical waveguides, such as optical fibers, are placed in close proximity, coupling is achieved. In this situation, the evanescent field generated by one of the fibers reaches the other fibers before decaying completely [28].

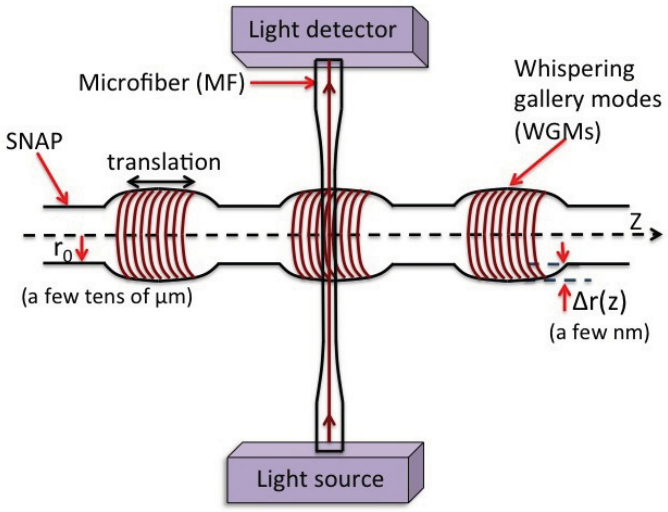

Figure 2.9: Coupling of light from a microfiber (MF) to a SNAP device.

As is shown in Figure 4.7, in order to couple light into a SNAP device, a microfiber is used as a waveguide to generate a strong evanescent field. When the SNAP device is close to the microfiber, the fiber's evanescent field produces propagating wave modes in the SNAP device. As a result, the light is coupled from the microfiber to the SNAP device. We will discuss more in the next chapter about the evanescent field of a tapered fiber.

2.3 Quantum analogy

In this section, we present a solution of Helmholtz's equation for an optical fiber as a dielectric waveguide. We will subsequently discuss formal analogies between the theory of SNAP and quantum mechanics.

2.3.1 Helmholtz equation

For a general waveguide with no free charge sources, the Helmholtz equation (Eq. 2.19) represents an eigenvalue problem for k with eigenfunctions $\vec{E}(\vec{r},\vec{k})$. Here, the eigenfunctions are called modes of the field. A time-dependent solution of this equation for harmonic fields in free space is a plane wave

$$\overrightarrow{E}(\vec{r},t) = \vec{E_0}\exp^{i(\vec{k}.\vec{r}-\omega t)} \tag{2.23}$$

where $\vec{k}$ is the propagation vector and $|k| = 2\pi/\lambda$.

In cylindrical coordinates, the gradient operator is given by $\nabla = (\widehat{\rho}\partial_\rho + \widehat{\varphi}\frac{1}{\rho}\partial_\varphi + \widehat{z}\partial_z)$. When considering the fields propagating along the z-axis of an optical fiber ($\vec{H_z}, \vec{E_z} \propto exp[-i\omega t]$), the cylindrical symmetry of the fiber allows us to express the Helmholtz equation as

$$(\partial_\rho^2 + \frac{1}{\rho}\partial_\rho + \frac{1}{\rho^2}\partial_\varphi^2 + \partial_z^2)\Psi + k^2\Psi = 0\ ,\ \Psi = E_z, H_z \tag{2.24}$$

There are two approximations we can make to simplify solving this equation. Firstly, we can assume that propagation in our system is based on WGMs; the field along the z-axis has a very slow variation, thus $\partial_z^2 = 0$. Secondly, we consider that $\Psi \propto \exp(-im\varphi)$ along the azimuthal direction, thus $\frac{1}{\rho^2}\partial_\varphi^2 = -\frac{m^2}{\rho^2}$, where m is the discrete azimuthal quantum number. These assumptions allow us to rewrite the equation in the form of Bessel's differential equation

$$\partial_\rho^2\Psi + \frac{1}{\rho}\partial_\rho\Psi + (k^2 - \frac{m^2}{\rho^2})\Psi = 0 \tag{2.25}$$

The general linear solution of this equation inside a cylindrical waveguide (e.g. the core of an optical fiber) for any integer, m, is defined by Bessel functions[29]

$$\Psi(k\rho) = c_1 J_m(k\rho) + c_2 Y_m(k\rho) \tag{2.26}$$

Outside of the core, the boundary condition for an infinite cladding require us to use combinations of Bessel functions, known as Hankel functions

$$H_m^{(1)}(k\rho) = J_m(k\rho) + iY_m(k\rho)\ ,\ H_m^{(2)}(k\rho) = J_m(k\rho) - iY_m(k\rho) \tag{2.27}$$

Definition of the boundary conditions leads to the eigenvalue equation. The eigenvalue equation for whispering gallery modes with a propagation constant of β and a wave number of $k = \frac{2\pi}{\lambda}$ in an optical fiber with refractive index of n_f and radius of r_0 is given by [30]

$$\Big(F_{1m}(U) + F_{2m}(W)\Big)\Big[F_{1m}(U) + \frac{n_0^2}{n_f^2}F_{2m}(W)\Big] = \Big[\frac{n\beta}{kn_f}\Big]^2\Big[\frac{V}{UW}\Big]^4 \tag{2.28}$$

where,

$$F_{1m}(x) = \frac{1}{xJ_m(x)}\frac{dJ_m(x)}{dx}\ ,\ F_{2m}(x) = \frac{1}{xH_m^{(2)}(x)}\frac{dH_m^{(2)}(x)}{dx} \tag{2.29}$$

and U, W and V are defined by

$$U = r_0(k^2n_f^2 - \beta^2)^{1/2}\ ,\ W = r_0(k^2n_0^2 - \beta^2)^{1/2}\ ,\ V = kr_0(n_f^2 - n_0^2)^{1/2} \tag{2.30}$$

The TE modes are given by

$$F_{1m}(U) + F_{2m}(W) = 0 \tag{2.31}$$

and for TM modes we have

$$F_{1m}(U) + \frac{n_0^2}{n_f^2} F_{2m}(W) = 0 \tag{2.32}$$

2.3.2 Analogy of guided optical modes and eigenstates

In this section, we discuss an analogy between the Helmholtz equation and Schrödinger's equation. To simplify the discussion, we consider the one-dimensional form of both equations.

2.3.2.1 Helmholtz equation

The general solution for guided waves is

$$E_z(x,t) = E_z(x)e^{-i\omega t} \tag{2.33}$$

$E_z(x)$ is a transverse eigenfunction of a guided mode that propagates along the z-axis ($E \propto e^{ik_z z}$) of a dielectric step-index waveguide with a core dimension of ($2d$). For distances between (d) and ($-d$), the refractive index is equal to n_1 (the core refractive index) and for distances greater than (d) or less than ($-d$), the refractive index is equal to n_2, the cladding refractive index. In this configuration, we can write the Helmholtz equation as

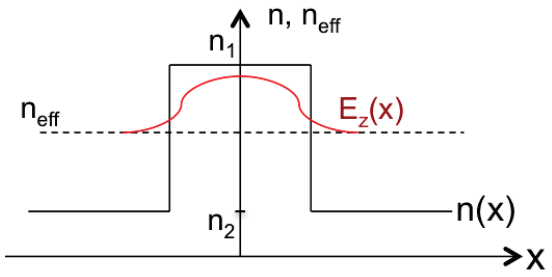

Figure 2.10: Solution of the 1D Helmholtz equation for a step-index dielectric waveguide.

$$\Big[\frac{d^2}{dx^2} + k_T^2\Big]E_z = \Big[\frac{d^2}{dx^2} + (k^2 - k_z^2)\Big]E_z = \Big[\frac{d^2}{dx^2} + \omega^2\mu\epsilon(x) - k_z^2\Big]E_z$$
$$= \Big[\frac{d^2}{dx^2} + k_0^2 n^2(x) - k_z^2\Big]E_z = 0 \qquad (2.34)$$

The eigenvalue $k_T = k^2 - k_z^2$ is the transverse propagation constant, where k_z is the longitudinal propagation state, also known as β, and $|k|^2 = \omega^2\mu\epsilon(x)$.

Figure 2.10 shows the solution to the one-dimensional Helmholtz equation in a step-index dielectric waveguide.

2.3.2.2 Time-independent Schrödinger equation

On the other hand, a time-independent Schrödinger solution for the wavefunction $\Psi(r)$ with an eigenvalue energy of E in a potential well is shown in Figure 2.11.

As you can see here, for distances less than $(-d)$ and greater than d, the potential is

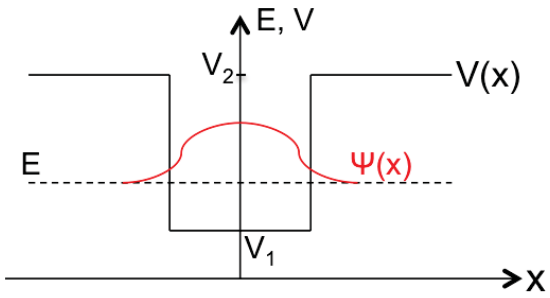

Figure 2.11: Time-independent Schrödinger solution in one-dimension.

V_2, and for distances equal to or less than d and $(-d)$, it equals V_1. The corresponding time-independent Schrödinger equation in 1-dimension is written as:

$$\left[\frac{-h^2}{2m}\frac{d^2}{dx^2} + V(x) - E\right]\Psi = 0 \tag{2.35}$$

with wavefunctions

$$U(x,t) = \Psi(x)e^{-i\frac{E}{\hbar}t} \tag{2.36}$$

Now, by comparing Equations 2.35 and 2.34, we can conclude that the potential $V(x)$ in Schrödinger's equation is equivalent to $-n^2(x)$ in the Helmholtz equation, while the energy E is equivalent to the propagation constant along the z-axis, k_z^2.

2.3.3 SNAP theory

Following this brief background, we can now explain SNAP theory. There are several approximations that we can apply to a SNAP device possessing a nanoscale variation

in radius (see Figure 2.12). We first assume that the field is propagating inside a SNAP fiber along the z-axis. Our second assumption is to suppose that there are no input or output waveguides in a SNAP fiber, so that the propagating field is based on the whispering gallery modes in a SNAP fiber. Finally, we consider the propagation of light to be adiabatic. This signifies that the effective radius variation of a SNAP varies slowly without perturbing the mode shape so that the scale of the propagating light does not change. In cylindrical coordinates (z, ρ, φ), the field distribution is defined as [25]

$$U_{m,p,q}(\vec{r}) = \Psi_{m,p,q}(z)\Xi_{m,p}(\rho)\exp(im\varphi) \tag{2.37}$$

where $\Psi_{m,p,q}(z)$ is the distribution of the WGMs along the z-axis and (m, p, q) are the discrete azimuthal quantum number, the discrete radial quantum number and the discrete or continuous axial quantum number, correspondingly. According to previous sections, if we apply this equation to the Helmholtz equation (Equation 2.19), we can write

$$(\nabla^2 + k^2)\Psi_{m,p,q}(z)\Xi_{m,p}(\rho)\exp(im\varphi) = 0 \tag{2.38}$$

To simplify this equation for cylindrical waveguides, we can use a transversal (x, y) and longitudinal (z) field decomposition. Therefore, the propagation constant (K) is written as

$$K^2 = K_T^2 + K_z^2 \tag{2.39}$$

where K_T and K_z are the transverse and longitudinal propagation constants, respectively. For a lossless propagating wave inside the core of an optical fiber, we can consider $K_z = \beta$. As a result, we can write

$$K^2 = K_T^2 + \beta^2 \tag{2.40}$$

Therefore, Equation 2.38 will be

$$\nabla^2(\Psi_{m,p,q}(z)\Xi_{m,p}(\rho)\exp(im\varphi)) + (k_T^2 + \beta^2)\Psi_{m,p,q}(z)\Xi_{m,p}(\rho)\exp(im\varphi) = 0 \tag{2.41}$$

Then

$$\begin{aligned}\Psi_{m,p,q}(z)\nabla_\perp^2(\Xi_{m,p}(\rho)\exp(im\varphi)) + (\Xi_{m,p}(\rho)\exp(im\varphi))\frac{d^2\Psi}{dz^2} \\ +K_T^2(\Psi_{m,p,q}(z)\Xi_{m,p}(\rho)\exp(im\varphi)) + \beta^2(\Psi_{m,p,q}(z)\Xi_{m,p}(\rho)\exp(im\varphi)) = 0\end{aligned} \tag{2.42}$$

We can split Equation 2.42 and rewrite it as

$$\frac{1}{\Xi_{m,p}(\rho)\exp(im\varphi)}\left[\nabla_{\perp}^{2}(\Xi_{m,p}(\rho)\exp(im\varphi))+K_{T}^{2}\right]\Psi_{m,p,q}(z) + \frac{1}{\Xi_{m,p}(\rho)\exp(im\varphi)}\left[\frac{d^{2}}{dz^{2}}+\beta^{2}\right]\Psi_{m,p,q}(z)=0 \tag{2.43}$$

By solving the equation above, we will find the one-dimensional Schrödinger equation to be

$$\frac{d^{2}\Psi}{dz^{2}}+\beta^{2}(\lambda,z)\Psi=0 \tag{2.44}$$

To find β, we use Equation 2.28. First, we consider a zero-order approximation where the propagation constant is zero. In this situation, from Equation 2.30, we can write

$$U_{0}=n_{f}kr_{0}\ ,\ W_{0}=n_{0}kr_{0} \tag{2.45}$$

Our second assumption is to suppose that the optical modes are propagating near the surface of the SNAP device. We can then write $U_0 \approx m >> 1$, $\Delta r = r - r_0$, and also $\Delta\lambda = \lambda - \lambda_{res}$, where λ_{res} is the resonant wavelength. When we apply these equations to Equations 2.30 and 2.19, we find

$$\beta(\lambda,z)=\left(\frac{2\pi n_{0}}{\lambda_{res}}\right)\left[\frac{\Delta r_{eff}(z)}{r_{0}}-\frac{(\lambda-\lambda_{res}-i\gamma_{res})}{\lambda_{res}}\right]^{1/2} \tag{2.46}$$

where γ_{res} is the material attenuation parameter, which in the case of silica is as small

as $10^{-3}\ pm$ [31]. Based on Schrödinger's equation 2.44

$$\beta^2(\lambda, z) = E(\lambda) - V(\lambda) \tag{2.47}$$

We can thus split Equation 2.46 into an energy part and a potential part. Considering

$$\beta_0 = \frac{2\pi n_{f0}}{\lambda_{res}} \tag{2.48}$$

and

$$\frac{\Delta r_{eff}(z)}{r_0} = \frac{\Delta r(z)}{r_0} + \frac{\Delta n_f(z)}{n_{f0}} \tag{2.49}$$

the effective energy, which is proportional to wavelength variation, is calculated as

$$E(\lambda) = -2\beta_0^2(\lambda_{res})\frac{\lambda - \lambda_{res} - i\gamma_{res}}{\lambda_{res}} \tag{2.50}$$

The effective potential is proportional to the variation of radius and refractive index, thus

$$V(z) = -2\beta_0^2(\lambda_{res})[\frac{n_{f0}\Delta r(z) + r_0\Delta n_f(z)}{r_0 n_{f0}}] \tag{2.51}$$

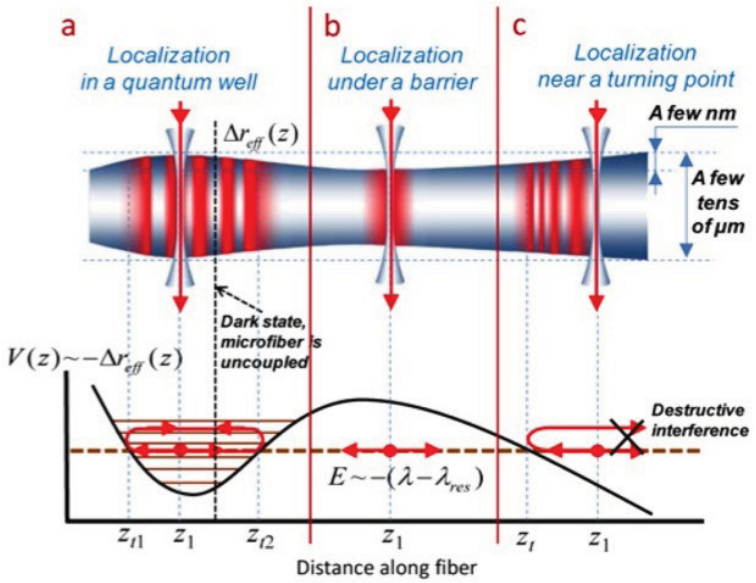

Figure 2.12: SNAP devices. **a.** WGM bottle microresonator. **b.** Concave fiber waist.**c.** Monotonic variation of fiber radius. [2].

2.3.4 "Quantum theory" of light in SNAP devices

SNAP devices can be divided into three different regimes, which are illustrated in Figure 2.12. The position of energy, (E), indicates the structure of a SNAP device similar to the three basic phenomena of quantum mechanics [32]. Here, it is proportional to the wavelength detuning from the resonator. The point z_1 shows the position of a microfiber along a SNAP fiber.

The first regime exhibits a bottle microresonator [33], which corresponds to a quantum well in quantum mechanics. When the microfiber is located in this regime, it leads to formation of the excited WGMs. The modes are restricted between tuning points of z_{t1} and z_{t2} at different series of wavelength, resulting in the formation of discrete states in this regime. At the point z_1, the amplitude of resonance transmission is

proportional to the amplitude of the WGM [2]. Also, if the microfiber is located at the node of WGM, no coupling occurs and the WGMs will be dark. These points are shown in Figure 2.12 as a dark state. Due to the effective radius variation of the SNAP device, waves which are launched in positive and negative directions along the SNAP device are reflected at the turning points z_{t1} and z_{t2}, resulting in constructive interference [34].

The second regime shows a shallow concave fiber waist, which corresponds to a potential barrier. If the energy is greater than the potential, corresponding to an energy found above the barrier, the WGMs excited in the SNAP device will not be localized. If the energy is less than the potential, corresponding to an energy found below the barrier, the amplitudes of the excited WGMs will exponentially decay from point z_1.

If the effective radius variation is equal to zero (implying a uniform fiber), the WGMs are delocalized. As a result, the excited WGMs in a uniform fiber radiate out along the axis of the fiber. However, we rarely see a resonant mode due to the self-interference of these Gaussian beams that occurs when they are rotating close to the surface. Also, the quality factor of this resonant mode is at least 2.5 times smaller than the equivalent modes in a spheroidal microresonator [35].

Finally, in the third regime, the radius of the SNAP device monotonically increases close to the point of z_1. In this regime, the excited WGMs propagating in the direction of decreasing radius (i.e. the negative direction along the SNAP device) from point

z_1 will interfere with the WGMs reflected from the turning point of z_t and, from the other side, the excited WGMs which propagate in the positive direction will undergo destructive interference. Therefore, the propagation of light is launched between the turning point z_t and the point z_1 in this regime [36].

Chapter 3

Fabrication

In this chapter, the fabrication of our devices is described. Our fabrication method has two main parts. First, we fabricate a microfiber that we can use as a waveguide to produce high evanescent fields. A high quality SNAP is subsequently fabricated as a microresonator. For all of these steps, we use a regular optical fiber. To begin, we will introduce current fabrication methods, including their advantages and disadvantages. We will then describe our experimental set-up and, finally, present our fabrication techniques.

3.1 Tapered fiber

In the past few decades, with the introduction of industrial optical fibers, an important goal of researchers has been to build micro- and nano-scale waveguide devices with low transmission losses. Among a wide variety of usable waveguides, microfibers (MFs)

have received greater attention due to their many interesting properties, including low transmission losses, easy fabrication, their ability to be assembled in three dimensions, strong coupling to optical systems, and their ability to produce a powerful evanescent field [31].

The first recorded effort for reducing the diameter of a fiber was achieved in 1887 by a British physicist, C. V. Boys [37]. He called it "a Finest Thread" of glass. Although the diameter of these fibers was less than one micrometer, their high degree of non-uniformity made them unsuitable for optical devices and guiding light. In 1959, N. S. Kapany was one of the first physicists who successfully used a fiber bundle composed of 275 optical fibers with diameters of 1 μm to transmit an image [38].

Nowadays, a lot of research is done in this domain and several techniques of fabrication are explained. The main property of a micro or a nano-fiber, used in many applications such as coupling to microresonators [39], is producing strong evanescent waves. Figure 3.1(a) shows a cross section of an optical fiber with a diameter greater than the wavelength of light λ. Light propagates along the fiber based on total internal reflection and is localized inside the core. The behaviour of light at the boundary of the core and cladding layers is explained by the Goos-Hänchen effect [30]. When the light hits the interface formed by the core and cladding layers, a fraction of the light penetrates the boundary as an evanescent field that exponentially decays into the external area. The reflected beam returns to the core with the Goos-Hänchen phase shift along its axial propagation direction. When the diameter of the fiber is reduced

to close the radiation wavelength λ, the evanescent field increases. This is due to the fact that the light has more reflection inside (Figure 3.1(b)). Finally, when the core diameter is smaller than the wavelength of light, a significant fraction of light can penetrate the boundary as an evanescent field (Figure 3.1(c)).

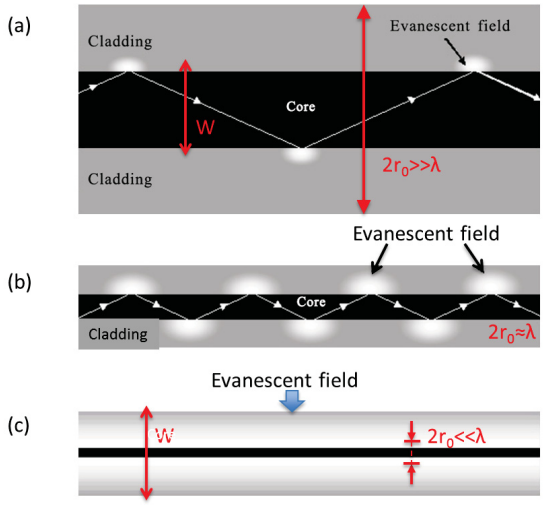

Figure 3.1: **a.** Fundamental mode in a regular optical fiber [13]. **b.** Fundamental mode in an optical fiber whose diameter is greater than the wavelength of the propagating light [13]. **c.** Evanescent field in a micro- or nanofiber with a diameter much smaller than the wavelength of light [13].

The width of the fundamental modes W is defined for mode characterization as $W = \frac{2}{\gamma_0}$, where γ_0 is the transverse propagation constant. Figure 3.2 shows the width of the evanescent field for a silica microfiber with $n = 1.46$ and $\lambda = 1530\ nm$ when the microfiber radius is much smaller than λ [31].

We can see that when the radius decreases, the width of the evanescent field increases significantly.

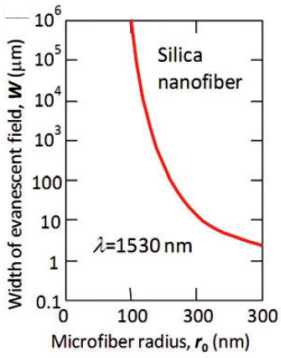

Figure 3.2: The width of the evanescent field versus the radius of the silica microfiber [31].

In general, the first principal condition for a high transmission tapered fiber is adiabaticity. Differences between an adiabatic and a non-adiabatic tapered fiber are shown in Figure 3.3 [40]. In a non-adiabatic tapered fiber, the fundamental mode may couple to the nearest higher order guided or radiation modes (take for example HE_{11} to HE_{12}). In this situation, a fraction of the energy in the higher order mode can interfere with the fundamental modes and cause high loss of power in a tapered fiber. As Figure 3.3 shows, loss of power is around $-0.6\ dBm$ [41].

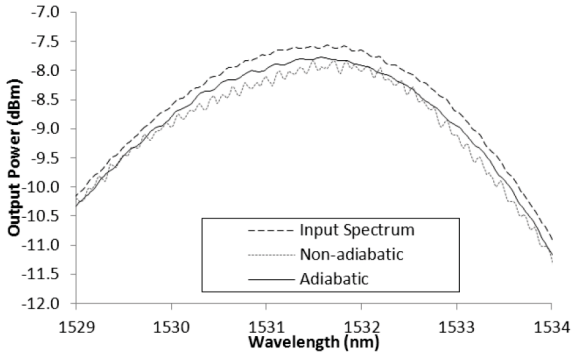

Figure 3.3: Transmission spectrum of a tapered fiber. Input spectrum (dashed), adiabatic taper (solid) and non-adiabatic taper (dotted) [40].

An adiabatic tapered fiber is based on the condition that the tapered fiber has a sufficiently small tapering angle Ω_z (See Figure 3.4). The tapering angle is defined as [30]

$$\Omega_z = \frac{r(z)}{z_b} = \frac{r(z)(\beta_1 - \beta_2)}{2\pi} \tag{3.1}$$

where $r(z)$ is the radius of the fiber core, z_b is the beating length of two adjacent modes, and β_1 and β_2 are the propagation constants of two adjacent modes.

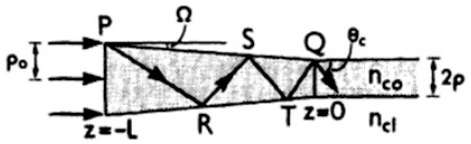

Figure 3.4: Schematic of a tapered fiber shows the adiabatic tapering angle. [30].

For a single mode fiber which supports only one mode, ($\beta_2 = 0$), therefore, the tapering angle could be large. Thus, a greater range of SMFs could satisfy the adiabatic condition. Correspondingly, for multimode fibers, if the different propagation between two neighboring modes is small, then the tapering angle will be small. Thus, an adiabatic MMF should have a smaller angle.

Another important condition is that tapered fibers should have a uniform waist.

3.1.1 Current fabrication

There are three common flame brushing configurations for fabrication of a low loss tapered fiber. All these methods are based on stretching an optical fiber while locally heating it with a flame. This process continues until a desirable diameter is achieved. In the following section, each one of these configurations is briefly explained.

The first design consists of two independent linear stages with a stationary heating source (See Figure 3.5). In this set-up, a flame is held motionless under the fiber and it heats a section of the fiber while the two stages move bidirectionally at the same time. This causes an oscillation of the fiber above the flame, while simultaneously elongating it. Due to the individual bidirectional motion of the stages, they must be aligned to prevent bending or jerking of the fiber, requiring more control of the set-up. Because the coupling motion, developing the control program is more involved [42].

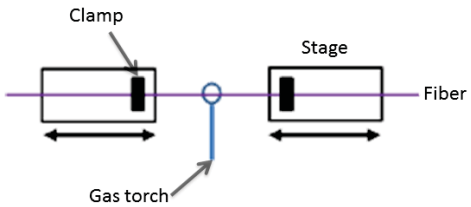

Figure 3.5: First configuration of a flame brushing rig: two independent linear stages with one motionless heating source [42].

In the second design, a fiber is fixed on two translation stages by two clamps. The stages stretch the fiber while the flame is installed on a third stage, where it sweeps along the fiber with constant speed (See Figure 3.6)[43]. Because the motion of stages

in this design are unidirectional and independent, control of the set up is easier and simple stepper motors can even be used. A disadvantage of this configuration is that, because of the motion of the heating source, the flame can be deformed, resulting in unpredictable results.

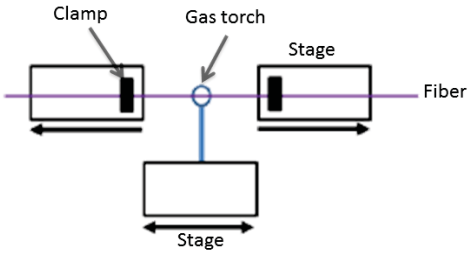

Figure 3.6: Second method of a flame brushing rig: two independent linear stages with one moving heating source [42].

The third method uses two linear stages on top of the other as a translator stage and a stretcher stage (See Figure 3.7). The flame is held stationary under the fiber. While the translator bottom stage is moving the fiber in front of the flame, the stretcher top stage is pulling the fiber until it reaches a desirable diameter [44, 45]. Although this method is an original technique of fabrication of a tapered fiber, there is the possibility of mechanical coupling between two stages. For instance, the load of the stretcher on the translator may cause inertia in the stretcher stage when it reverses direction, possibly causing bending of the fiber [46].

Between all the methods which were explained and considering the advantages and disadvantages of each configuration, we chose the last one. We have thus installed this system and have developed a control program for the bidirectional motion of the

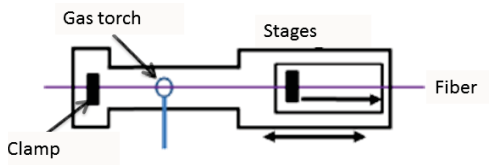

Figure 3.7: Third method of a flame brushing rig: two linear stages on top of each other with one motionless heating source [42].

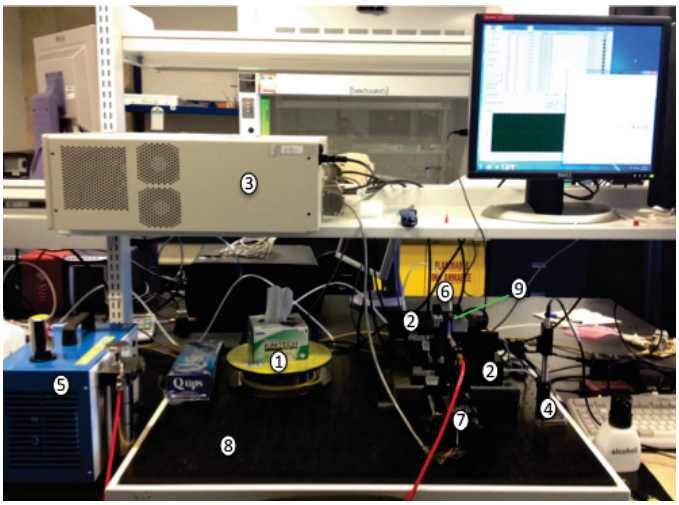

Figure 3.8: Overview of the microfiber fabrication station. Details are given in Table 3.1.

translator stage and unidirectional motion of the stretcher stage.

3.1.2 Design

Figure 3.8 shows our fabrication set-up used to make tapered fibers; each component is introduced in Table 3.1.

A schematic of the experimental set-up is shown in Figure 3.9. The translator and stretcher stages which are installed on top of each other are shown with (A). The flame

Table 3.1: Components of the pulling system

number	Component	Company	Description
1	**Fiber**	Corning	$SMF28E$
2	**Stages**	Newport	$XMS100$
3	**Controller**	Newport	$XPS-Q8$
4	**Photo-diode Detector**	Thorlabs	$PDA-10CF$ InGaAs
5	**Torch**	SRA	250 H_2O Welder
6	**Fiber Clamp**	Thorlabs	$T711/M-250$
7	$1D$ **Stepper motor**	—	—
8	**Optical breadboard**	—	—
9	**Nozzle**	Zoro	30 Gauge/Dispense needle

is held on a 1D stepper stage which is shown as (B). It is used for torch movement to put the flame at the right position or exactly under the fiber and to take it out when the process is completed.

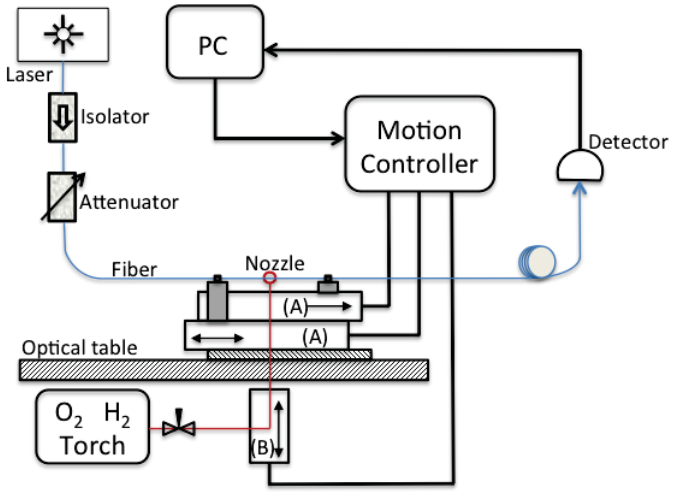

Figure 3.9: A schematic of a fiber pulling rig system.

Before starting the fiber pulling process, de-stressing of the fiber is useful. Commercial fiber is fastened tightly around a drum. When it is unwound and held tightly with

the clamps, there is a possibility that fiber still has curvature and tension. Heating the fiber then causes the strain to release. As a result, the fiber deflects and its transmission reduces. Thus, it is a necessary to straighten the fiber after unwinding [42].

Secondly, the protective plastic jacket of the fiber has to be removed (the striped length is around 15 mm). The naked fiber is then cleaned with a wiper or a cotton Q-tip and 99% IPA alcohol to completely remove dust and the remnant of the plastic jacket. Otherwise, the flame will burn them immediately and will result in a non-uniform waist with high losses on the tapered fiber. After these steps, the fiber is mounted straight in two magnet clamps on top of the translation stages. The clamps supply strong force to hold the fiber with diameters between 250 μm and 125 μm without bending or crashing it.

Due to the microporous structure of silica, it can absorb water up to 22% [47]. Thus, it is better to install the pulling rig system in a very clean room with low humidity. Using a clean-room box or a fan will be useful. During the process, the fan should be turned off to avoid vibrations or air currents.

In our design, a hydrogen-oxygen torch is used as a heating source. Other common heating sources used are an oxy-butane torch [48], CO_2 laser [49, 50], or an electric strip heater [51]. Each of them has their own advantages and disadvantages. For example, if oxygen is abundant in an oxy-butane torch, butane (C_4H_{10}) burns into CO_2 and H_2O. However, when oxygen is limited, carbon soot will be formed, resulting

in impurities on the surface of the fiber which will introduce losses or even burn the waist. CO_2 lasers are very stable and a suitable source of heat, but focusing the laser beam on the fiber is not easy. In addition, there are limits on the achievable thinness due to the decreasing absorption of cross-section. During the pulling process, appropriate temperatures are between 1200^oC to 1470^oC. The temperature should be above the annealing temperature of glass (i.e. 1200^oC) to allow the optical silica fiber to start softening, but below 1470^oC. Above that temperature, amorphous (non-crystalline) silica may crystalize. Usually, optical fiber is composed of amorphous silica. The high temperature may cause the formation of $\beta - cristobalite$ with a hexoctahedral crystal system, which has a higher density and refractive index [52]. Thus it reduces the transmission of the tapered fiber. Table 3.2 gives an overview of the properties of these two silica systems.

Table 3.2: Some properties of SiO_2 amorphous and poly-morphs: $fused\ Silica$ and $\beta - cristobalite$ [53, 54, 55]

Name	$fused\ silica$	$\beta - cristobalite$
Formula	SiO_2	SiO_2
Color	colorless	colorless
Specific Density (g/cm^3)	2.2	2.27
Refractive index	1.4585	1.479
$Si-O$ **Distance** (nm)	$0.159 - 0.162$	0.151
$Si-O-Si$ **Angle**	144^o	148^o
Crystal system	amorphous	cubic
Crystal class	—	hexoctahedral

A hydrogen-oxygen torch produces the suitable temperature with lower gas flow rate. Therefore, there is less pressure on the tapered fiber and it is one of the advantages

of the hydrogen-oxygen torch as a heat source.

The last important thing about the set-up is the distance between the tip of the torch and the fiber. If the fiber is far from the flame, it will not receive enough heat, and it will not soften. If the fiber is too close to the tip of the torch, it will receive too much heat and it will start to melt. In our design, we have determined the appropriate distance to be around 4.3 mm.

After setting up the apparatus successfully, we are ready to make a tapered fiber with a desirable diameter. A computer program is written to control the process (See Figure 3.10).

In this program, "Pulling speed" is the speed of the pulling or the speed of the top stage. "X sweeping speed" is the speed of the bidirectional motion of the bottom stage. During the process, these two items can not be changed. At the beginning of the process, "Enable Motors" causes the controller to initialize the three stages and put them in the right position to start the process. Then, when the process starts, the linear stage will start moving and the torch will approach a suitable position under the fiber. "Torch Y base position" shows the distance between the needle and the fiber in millimetres. After the "Hot zone length" is given, the total process is divided into four steps. During the first step, from 0 to 155 s, pulling starts from 6 mm to 8 mm. During the second step, the hot zone length is constant at 8 mm for 246 s. Then, for the third step, pulling is changed from 5 mm to 10 mm during 268 s. Finally, the hot zone length is fixed at 9 mm. In this recipe, after 1100 s, we start to increase

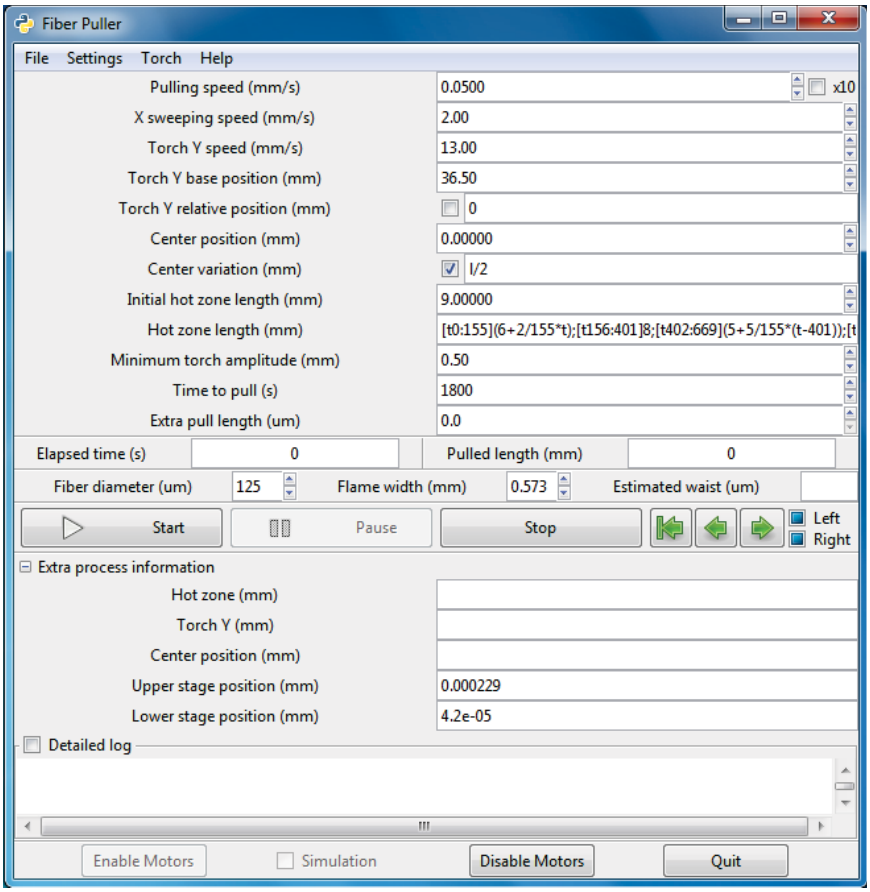

Figure 3.10: The graphical interface of our program to control the process.

the distance between the nozzle and the fiber very slowly in 10 μm steps every 70 s. Depending on the conditions, it might be sometimes necessary to stop the program before 1800 s. Generally, at any desirable time, the program can be stopped. The diameter of the tapered fiber can be measured with an optical microscope. Through trial and error, several different recipes were found to give various desired diameters (see Appendix A).

To better understand this recipe, "the reverse problem" [56] should be reviewed. In 1992, Briks *et al.* first described a model for exponential and linear transition shapes of tapered optical fibers of varying lengths [56]. Due to the easier design and more control over the taper angle (Ω_z), the linear taper received more attention.

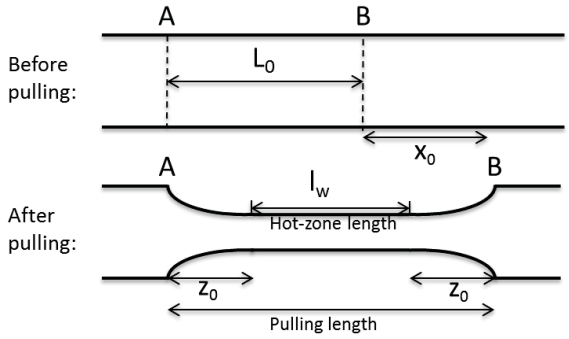

Figure 3.11: Schematic of the fiber pulling before and after the pulling process.

According to the "reverse problem", the desirable shape of the tapered fiber is specified and $L(x)$ and x_0 are required. Here x_0 is a final elongation and $L(x)$ is a function of elongation. In this method the final elongation is determined by [56] (see Figure 3.11)

$$x_0 = 2z_0 + l_w - L_0 \tag{3.2}$$

When the hot-zone length is changed linearly with the taper elongation, the linear hot-zone length is given by [56]

$$l_w = L_0 + \alpha x_0 \tag{3.3}$$

where l_w is the length of the taper waist, L_0 is a constant hot-zone and α is a relative amount of hot-zone change to taper extension [56].

From these two equations (Eqs. 3.2 and 3.3), α can be written as

$$\alpha = 1 - 2(\frac{z_0}{x_0}) \tag{3.4}$$

Because z_0 is always $\leq x_0$, $\alpha \leq 1$. When the taper transition length z_0 is equal to x_0, then $\frac{z_0}{x_0} = 1$ and $\alpha = -1$. Correspondingly, when $z_0 = 0$, $\alpha = 1$. In Figure 3.12, the various taper shapes from a linearly different hot-zone length are shown[56].

In our design, in the second and last steps we consider $\alpha = 0$, in the first step $\alpha = 0.26$ and in the third step, α is defined as 0.37.

During the pulling process, transmission is monitored by an amplified detector. The data is controlled and is recorded by a program in the computer (See Figure 3.13).

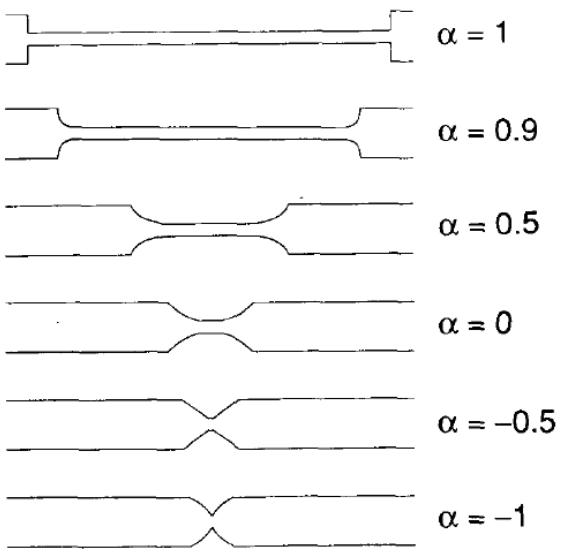

Figure 3.12: The different taper shapes are shown for varying values of α [56].

From the ratio of the final transmission to the initial transmission of the process, we can find out the fractional loss.

We start our experiment using previously known recipes. According to our set-up, we have determined the new α. Now, we are able to make a single mode tapered fiber with diameter of $1 \sim 2\mu m$ and we have reached the maximum transmission of 98% with these recipes.

Using the first recipe, as explained before, we have been able to make a tapered fiber with a total extension of around 75 mm, which gives us a transmission above 85% . For our experiment, transmission above 60% is enough to generate strong evanescent field.

We also developed another recipe ($\alpha_1 = 0.13$ and $\alpha_3 = 0.19$) which gives us a smaller

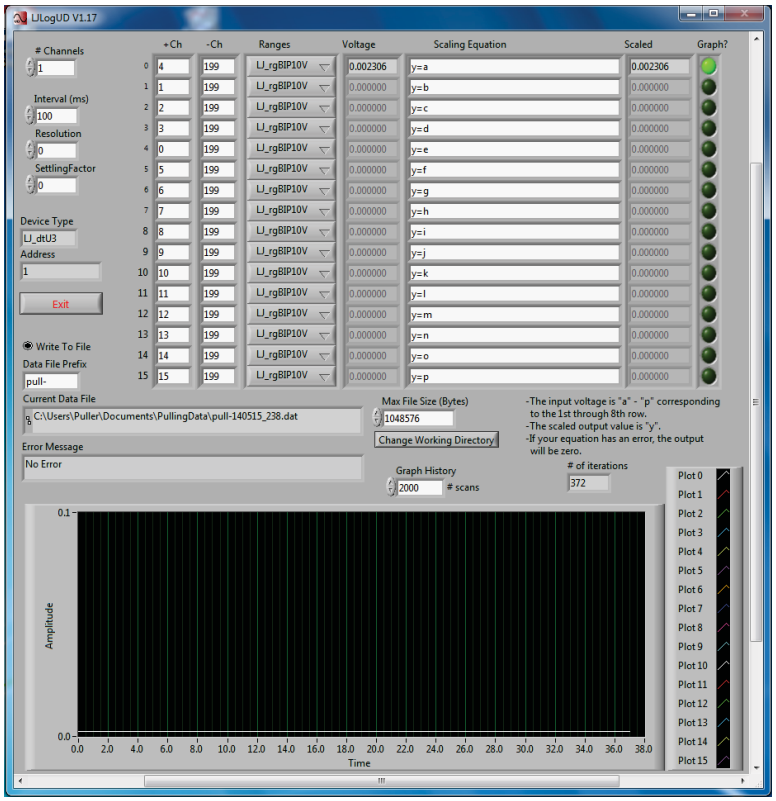

Figure 3.13: The graphical interface of our programme for monitoring the transmission during the process.

hot zone length and a single mode microfiber with a regular transmission of more than 90% and a total extension of around 80 mm, as shown in Table 3.3.

Table 3.3: Recipe to make a tapered fiber with a pulling length of 4.5 mm

Pulling speed (mm/s): 0.05	Torch speed (mm/s): 13
Torch Y base position (mm): 35.80	Center position (mm): 0
Initial hot zone length (mm): 9	X sweeping speed (mm/s): 2
Minimum torch amplitude (mm): 0.5	Center variation (mm): 1/2
Pulling (mm)	Duration (s)
From 3 to 4	155
At 4	256
From 2.5 to 5	268
At 4.5	231
[t0:155](3+1/155*t);[t156:401]4;[t402:669](2.5+2.5/155*(t-401)); [t670:900]4.5;	

After fabricating a tapered fiber that produces a strong evanescent field, the fiber is transferred to the characterization set-up.

3.2 SNAP

Having now discussed the tapering of optical fibers, a discussion concerning the fabrication of the SNAP structures follows.

3.2.1 Current methods

Two techniques were originally introduced for the fabrication of SNAP device; IR beam exposure and UV beam exposure [57].

IR beam exposure

The first method is based on modification of the density and refractive index of the tapered fiber material by annealing. In this set-up, a fiber is first tapered to a small diameter $10-50\ \mu m$. A CO_2 laser beam is then focused on the surface of the tapered fiber (see Figure 3.14). Due to absorption of the laser light, heating causes a local annealing of the fiber, resulting in changes in the density and refractive index of the fiber. [52].

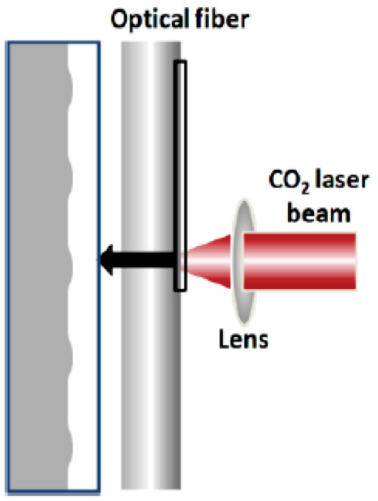

Figure 3.14: First fabrication method of SNAP device with IR (CO_2 laser) beam exposure [58].

This method is applicable for a variety of glass fibers [3].

UV beam exposure

This method is based on the modification of the refractive index and density of a fiber by UV beam exposure. A photosensitive Germanium (Ge)-doped, coreless tapered fiber is needed. An excimer laser beam with a wavelength of 248 nm is radiated to

the fiber through an amplitude mask with the desired pattern of a 300 μm period (see Figure 3.15). The bottle microresonators created by this method are very shallow, with an axially asymmetric effective radius variation of 0.5 nm.

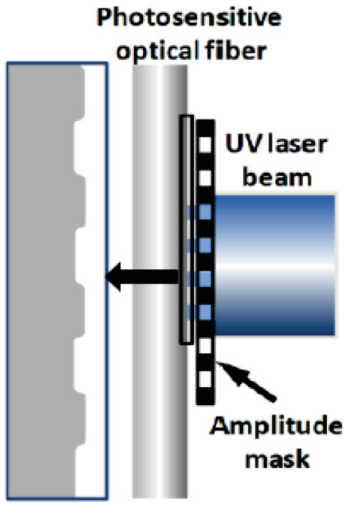

Figure 3.15: Second fabrication method of SNAP device with UV beam exposure [58].

Due to formation of GeOHC at around 240 nm, this kind of fiber demonstrates substantial absorption at UV wavelengths [59], showing significant attenuation. As a result, the effective radius variation at the front fiber surface is different than the effective radius at the back fiber surface. In spite of this, the UV beam exposure method allows for a very accurate variation of the fiber's effective radius.

3.2.2 Motivation

Although current fabrication methods are accurate in producing a variation in the fiber's effective radius, these methods require equipments that might not be easily

available, such as a CO_2 laser or photosensitive fibers. Thus, we present a new fabrication method of SNAP devices that uses only a regular hydrogen-oxygen torch. Our fabrication method is low cast and very straight-forward to implement.

3.2.3 Design

Our fabrication method has two steps. The first step is tapering the fiber to a smaller diameter. In this step, we use the "flame-brush" technique explained in the previous section. Figure 3.16 shows a schematic of this process.

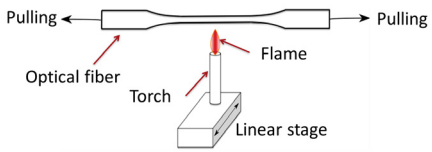

Figure 3.16: A schematic of tapering of the optical fiber.

A regular optical fiber is pulled while a sweeping flame softens it. Starting from the diameter of a regular optical fiber of 125 μm, we reduce the diameter to around 22 μm. The recipe and parameters used for this diameter with a pulled length of 25.5 mm are described in Table 3.4.

We have chosen this particular diameter according to coupling spectra results. The spectra of SNAP devices with diameters greater than 22 μm show coupling to more modes and they are very crowded. Alternatively, SNAP devices possessing smaller diameters are not easy to couple to microfibers. Figure 3.17 shows a tapered fiber

Table 3.4: First step of making a SNAP device: a tapered fiber with diameter 22 μm and pulled length of 25.5 mm

Pulling speed (mm/s): 0.05	Torch speed (mm/s): 13
Torch Y base position (mm): 35.80	Center position (mm): 0
Initial hot zone length (mm): 9	X sweeping speed (mm/s): 2
Minimum torch amplitude (mm): 0.5	Center variation (mm): 1/2
Pulling (mm)	Duration (s)
From 6 to 8	61
At 8	175
From 5 to 10	158
At 9	273
[t0:61](6+2/61*t);[t62:236]8;[t237:394](5+5/61*(t-236));[t395:509]9;	

with a radius of 55 μm fabricated in our lab.

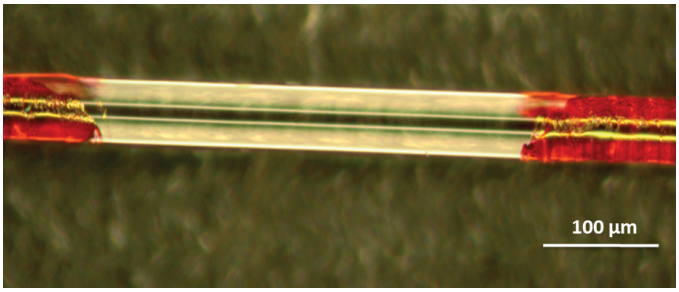

Figure 3.17: A microscopic image of a microfiber with radius of 55 μm.

For our second step after pulling, we pass the torch at a specific position of the tapered fiber. We set the pulling program using the parameters specified in Table 3.5. Depending on how many times we want the torch to pass under the fiber, the parameter of "Torch Y base position" is changed. When the nozzle reaches a position of 45 mm (the maximum amount of motion for the 1D stepper stage on which the flame is installed on it and, as a result, the maximum distance of the flame with the fiber in the side of the stage in our set-up), we can turn off the torch before stopping

the program. Otherwise, it will pass more than one time under the fiber. It is also possible to pass the torch more than once through the fiber. For example, when the nozzle reaches to position of 45 mm, we set this parameter to 25 mm and then again we switch to 45 mm to make three passes.

Table 3.5: Parameters of the pulling program for the fabrication of a SNAP device

Pulling speed (mm/s): 0	Torch speed (mm/s): 8
Torch Y base position (mm): 45	Center pulling (mm): 7.5
Initial hot zone length (mm): 0	Hot zone length (mm): 0
Minimum torch amplitude (mm): 0	Center variation (mm): 0

The parameter "Torch speed" also has an effect on the effective radius variation of the SNAP device. Depending on how much time we want the torch to spend under the fiber, the parameter of "Torch speed" is changed.

Any radius variations produced by the local connecting are on the nanoscale. Figure 3.18 shows the SEM image of one of our SNAP devices, where it is impossible to determine a change in the physical radius.

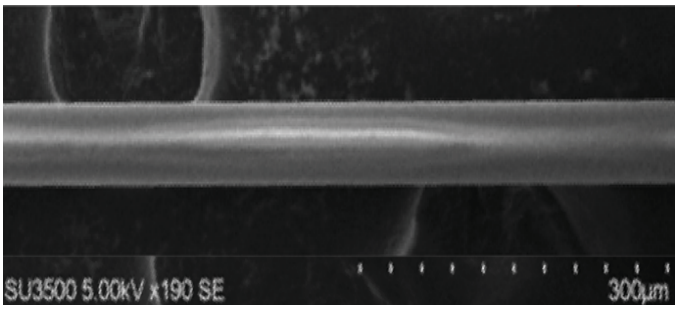

Figure 3.18: A scanning electron microscope (SEM) image of a SNAP device.

Chapter 4

Characterization

After fabricating a microfiber and a SNAP device, we characterize them to confirm the presence of a nanoscale effective radius variation. Characterization of these devices through precise measurement can be very useful to improve the devices. For example, with accurate measurement of the effective radius variation of a tapered fiber, an optimized pulling process can be developed. Two characterization methods have been introduced, with angstrom [31] or sub-angstrom [60] precision. Because of the cylindrical geometry of microfibers and SNAP devices, common methods of characterization such as atomic force microscopy (AFM), transmission electron microscopy (TEM), or scanning electron microscopy (SEM) are not applicable.

In this thesis, the method of characterization with sub-angstrom precision is used. The first method, with angstrom precision, is used more for the characterization of a tapered fiber. The experimental set-up is shown schematically in Figure 4.1. In this method, a light source and a light detector are connected to the microfiber directly.

The microfiber is placed in a linear stage with two translational axes, x and z. It moves along the z-axis of the SNAP device while touching the SNAP fiber at periodic positions. At each of these positions, the transmission is measured.

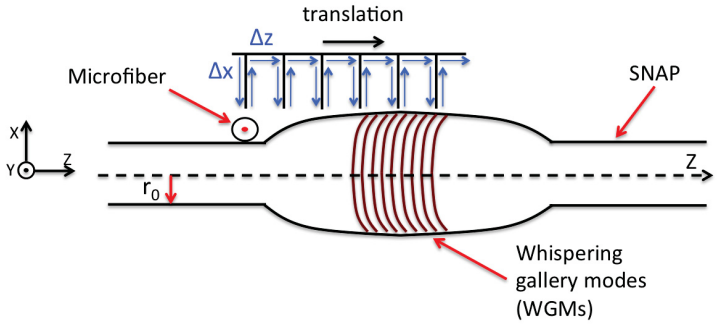

Figure 4.1: A schematic of characterization of SNAP fiber with sub-angstrom precision.

At each step of measurement, while the microfiber has a distance Δx (along the x axis) from the SNAP fiber, the microfiber is moved by Δz along the SNAP device and is then translated along x until it touches the SNAP fiber. The transmission spectrum is measured at this position. The microfiber is subsequently moved back by Δx along the x axis from the SNAP device to prepare for a new step of measurement.

Coupled light corresponds to WGMs travelling close to the surface around the circumference of the SNAP fiber. The radiation, or free space, wavelength of light, λ, for coupled WGMs is [61]

$$\lambda = \frac{2\pi r_0 n_f}{m} \tag{4.1}$$

where r_0 and n_f are the radius and refractive index of the SNAP device, respectively.

The integer m is the azimuthal mode number corresponding to the number of 2π phase changes around the circumference of the SNAP device [62]. Since the path of the light inside the SNAP device is close to the interface and its length is much larger than λ, m will be a large number.

If we expand λ to $\lambda + \Delta\lambda$a and r to $r + \Delta r$, we can rewrite equation (4.1) as

$$\frac{2\pi r n_f}{\lambda} = \frac{2\pi}{(\lambda + \Delta\lambda)} n_f (r + \Delta r) \tag{4.2}$$

Thus, we can write

$$\frac{r}{\lambda} = \frac{r}{\lambda + \Delta\lambda} + \frac{\Delta r}{\lambda + \Delta\lambda} \tag{4.3}$$

When we expand $\frac{1}{\lambda+\Delta\lambda}$, to $\frac{1}{\lambda}(1 - \frac{\Delta\lambda}{\lambda})$, we will have

$$\frac{r}{\lambda} = \frac{r}{\lambda}\Big(1 - \frac{\Delta\lambda}{\lambda}\Big) + \frac{\Delta r}{\lambda}\Big(1 - \frac{\Delta\lambda}{\lambda}\Big) \tag{4.4}$$

We can rewrite this equation as

$$0 = -\frac{\Delta\lambda}{\lambda} + \frac{\Delta r}{r} - \frac{\Delta r \Delta\lambda}{r\lambda} \tag{4.5}$$

Finally, we are assuming that the radius of the SNAP device is changing very slowly (i.e. $\Delta r \longrightarrow 0$) and that $\Delta\lambda \longrightarrow 0$. The radius variation of the fiber is calculated from [60]

$$\Delta r = r\frac{\Delta\lambda}{\lambda} \tag{4.6}$$

where $\Delta\lambda$ is the shift of a resonant peak. We can rewrite the equation (4.6) as

$$\Delta r_{eff}(z) = (\lambda_{res}(z) - \lambda_{res}(0))\frac{r_0}{\lambda_{res}} \tag{4.7}$$

where $\lambda_{res}(z)$ is the wavelength of the resonant peak, the radius is equal to $(r_0 + \Delta r_{eff}(z))$, and $\lambda_{res}(0)$ is the wavelength of the resonant peak where the radius is equal to r_0.

Equation (4.7) shows that if we have an accurate transmission spectrum of the tapered fiber, we are able to easily find the the effective radius variation of the SNAP device. Unfortunately, we can not get a exact spectrum in our set-up due to jitter in the wavelength during the measurement. In our transmission spectra, the resonant peaks shift randomly. To solve this problem, we have a plan to add a wavelength scale to our set-up. We will then be ready to estimate the effective radius variation of the fabricated SNAPs.

In the following section, our measurement set-up and results are explained.

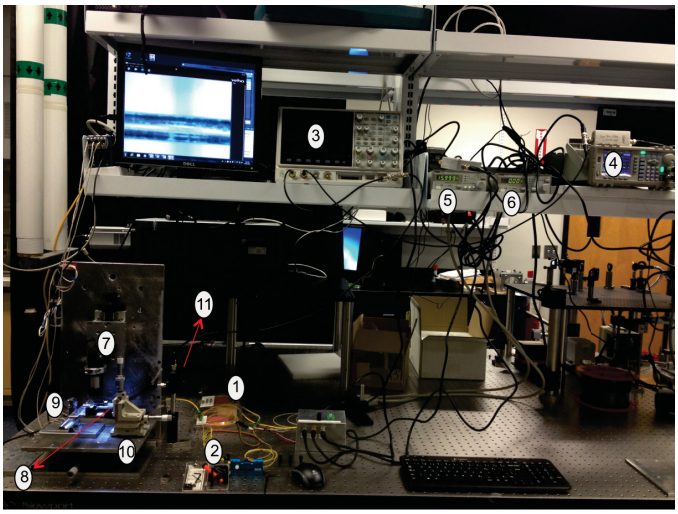

Figure 4.2: Overview of the SNAP fiber characterization station. Details are given in Table 4.1.

4.1 Instrumentation

Figure 4.2 shows the set-up used to characterize the SNAP fiber; each component is introduced in Table 4.1. A schematic of the experimental set-up is shown in Figure 4.3.

After fabricating a tapered fiber and a SNAP device, we transfer them (with the detector) to the characterization set-up. A tapered fiber with a diameter of less than 2 μm is placed on a linear, three-axis translation stage. We control the motion of this stage through a computer program (see Figure 4.4).

We use the tapered fiber as a waveguide to generate a strong evanescent field. In chapter 3, we mentioned that the evanescent field decreases exponentially away from the surface of a tapered fiber. Thus, coupling the light to a SNAP fiber through a

Table 4.1: Components of the characterization system

number	Component	Company	Description
1	**Optical Isolator**	E-TEK	1480/1550 nm EDFA
2	**Optical Attenuator**	OZ Optics	$172766-001$
3	**Oscilloscope**	Tektronix	MDO $4000B$
4	**Function Generator**	Atten	$ATF20B$ DDC
5	**Temperature Controller**	Thorlabs	TED $200C$
6	**Laser Diode Controller**	Thorlabs	LDC $200C$
7	**Optical microscope**	Veho	—
8	**Piezo Disk Scanner**	home made	–
9	**Accurate stage**	Micronix USA	$PPS-20$ ($\times 3$)
10	**Manually stage**	—	—
11	**Photo-diode Detector**	Thorlabs	$PDA-10CF$

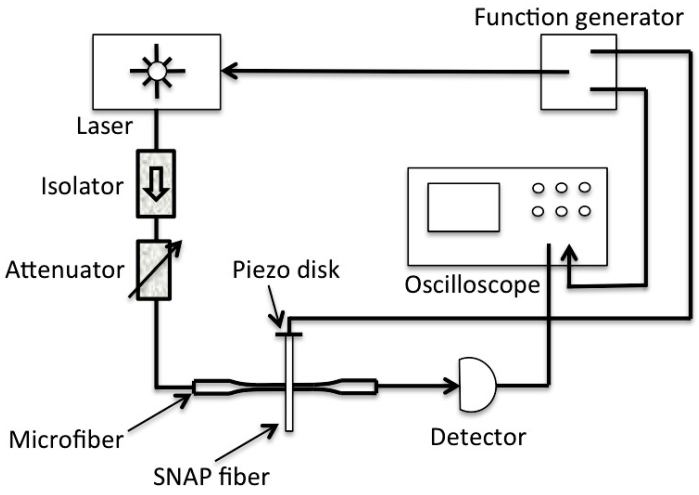

Figure 4.3: A schematic of the characterization set-up of a SNAP device.

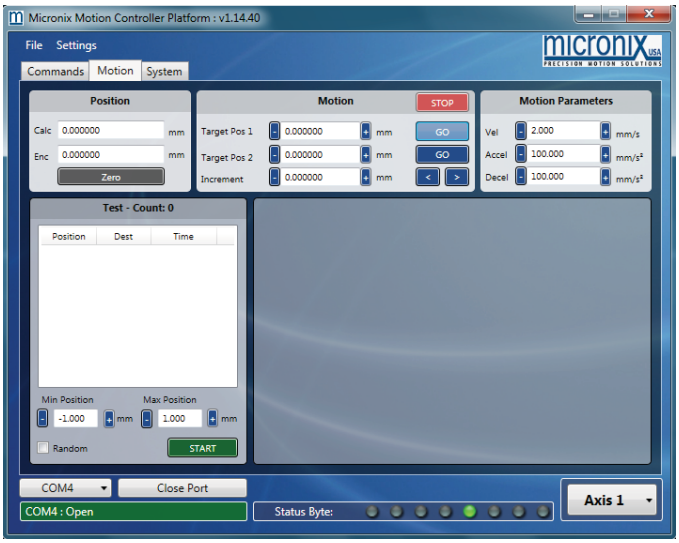

Figure 4.4: The graphical interface of our program for accurate motion control of the stage.

tapered fiber requires exact control of the distance between them. In this set-up, a home-made piezo disk scanner (see Figure 4.5) is used to precisely control this distance.

The SNAP fiber is connected magnetically to the piezo, which is mounted on a linear translation stage. The position of the piezo disk can be changed within a range of several micrometers by applying a voltage to the piezo scanner driver. This voltage is generated by a digital-to-analog device controlled by a computer. Figure 4.6 shows the program that controls the voltages for the piezo disk scanner. There are two buttons that go directly to the maximum and minimum voltages of the device. It is also possible to directly enter voltages into the box.

We use a function generator to generate a signal source such as a triangle, sine or

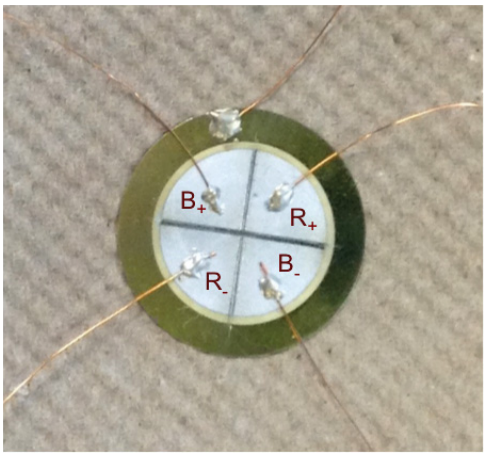

Figure 4.5: A Piezo Disk Scanner.

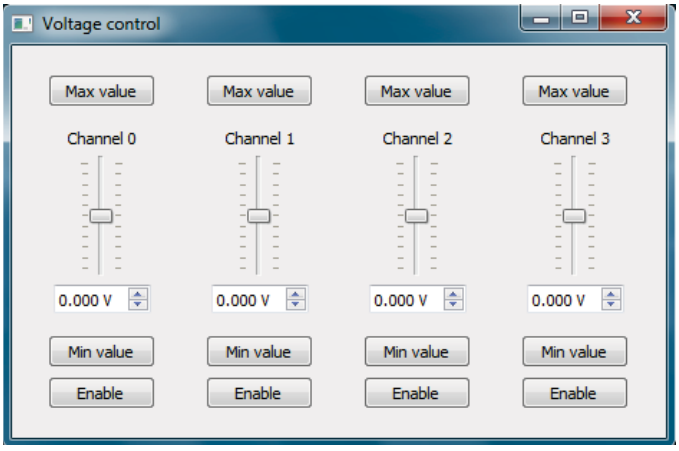

Figure 4.6: The graphical interface of our program for the motion control of our home-made piezo.

square waveform, to provide a specific voltage over a specific time. This signal is used to modulate the intensity of the current of the diode laser. We generally use a triangle wave with a peak-to-peak voltage of $2v_{pp}$ and a frequency of 10 Hz. Therefore, we scan from low voltage to high voltage and then from high voltage to low voltage. We send the light from a Telecom infra-red laser with a center wavelength of $\lambda = 1589\ nm$ to the tapered fiber and detect the transmitted light at the end of waveguide with a photodetector. The photodetector voltage is sent to an oscilloscope to measure the intensity of the transmitted light in the tapered fiber.

When the SNAP fiber is close to the microfiber, a portion of the light is coupled to it. When we observe the transmission spectrum at different wavelengths, we see transmission drops at specific λ, indicating the presence of coupling resonances at these wavelengths. Figure 4.7 shows a microscopic image of a SNAP fiber on the top of a tapered fiber.

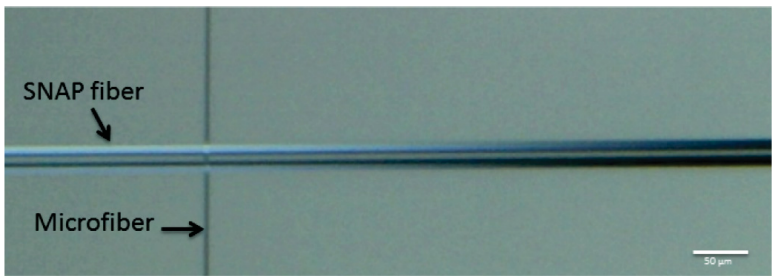

Figure 4.7: A microscopic image of a SNAP fiber with radius of 22 μm on the top of a tapered fiber.

4.1.1 Data processing

Our raw data is a function of voltage over time. To convert the raw data to a normalized transmission over wavelength, the following sequence is run:

1. The output current is calculated using $voltage \times 50\ A/V$. The conversion coefficient depends on the maximum values of voltage and current, which have been found to be 50 A/V for our laser diode driver.

2. After calibrating our laser, we calculate a conversion function for the wavelength in terms of the current

$$\lambda = 1589.38583 + 0.00258 \times I + 2.38561 \times 10^{-5} \times I^2 \quad (nm) \tag{4.8}$$

Using the values of I from the previous step in Equation (4.8), the abscissa is converted to wavelength. The data at this point has the units of voltage versus wavelength.

3. Zero subtraction normalization

To increase the efficiency of the process, we use several scripts to process the data (See Appendix B). The order of these scripts are:

1. make-tc-cal.py

This script uses the temperature and the value of current of the our telecom laser diode (based on a calibration made with an Optical Spectrum Analyser) to create a calibration file.

2. MDO-to-scope.py

This script takes a data file recorded directly from the oscilloscope and prepares it for the next script.

4. extract-scope.py

This script processes a data file from past scripts with the calibration file and saves a new data file consisting of two columns: wavelength (nm) and normalized transmission.

4.2 Characterization results

Figure 4.8 shows the spectra obtained from a SNAP device by scanning along the microfiber along its axis. At different spatial positions, we can observe distinct patterns in the spectra, corresponding to coupling to different axial modes.

From this figure, we can infer that the spatial extent for the SNAP device along the microfiber is no more than 450 μm (from point B to point H). The distance between two subsequent measurement steps (e.g. from point A to point B) is 75 μm.

4.3 Quality factor

The concept of quality factor was defined in chapter 2. In this section, we use this description to calculate the quality factor for some of our spectrum results. Figure

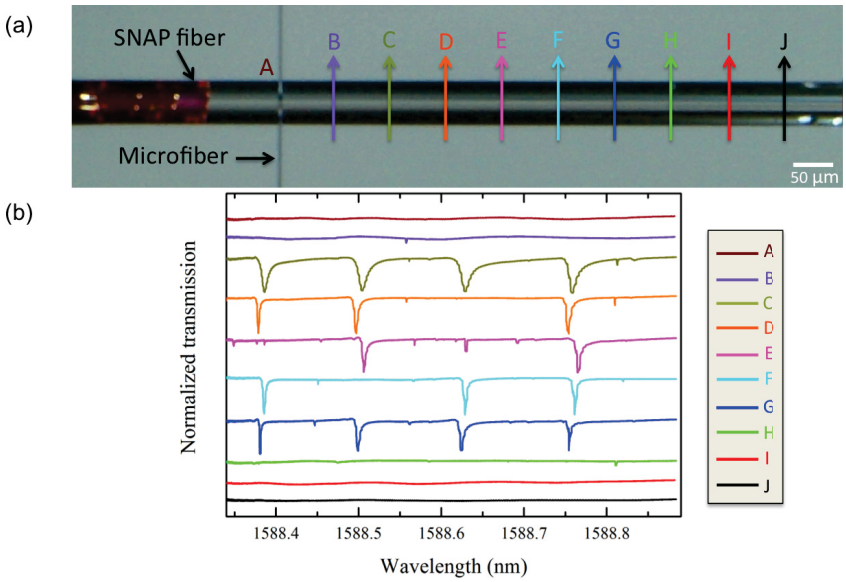

Figure 4.8: **a.** A microscopic image of a SNAP device and a tapered fiber and different measurement steps along the SNAP device. **b.** Distinct spectra of a SNAP device at different spatial positions.

4.9 shows the spectra of two different SNAP devices that we made in our lab. Very narrow transmission lines indicate low optical losses.

From Equation (2.7), the quality factor of each of these SNAPs are calculated as

$$\textbf{SNAP (a)}: \qquad Q = \frac{\lambda_c}{\Delta\lambda} = \frac{1588.5626445065 \ \ (nm)}{2.6513868587 \times 10^{-5} \ \ (nm)} = 5.99 \times 10^7 \qquad (4.9)$$

and also

$$\textbf{SNAP (b)}: \qquad Q = \frac{\lambda_c}{\Delta\lambda} = \frac{1588.56505 \ \ (nm)}{9.98417 \times 10^{-5} \ \ (nm)} = 1.6 \times 10^7 \qquad (4.10)$$

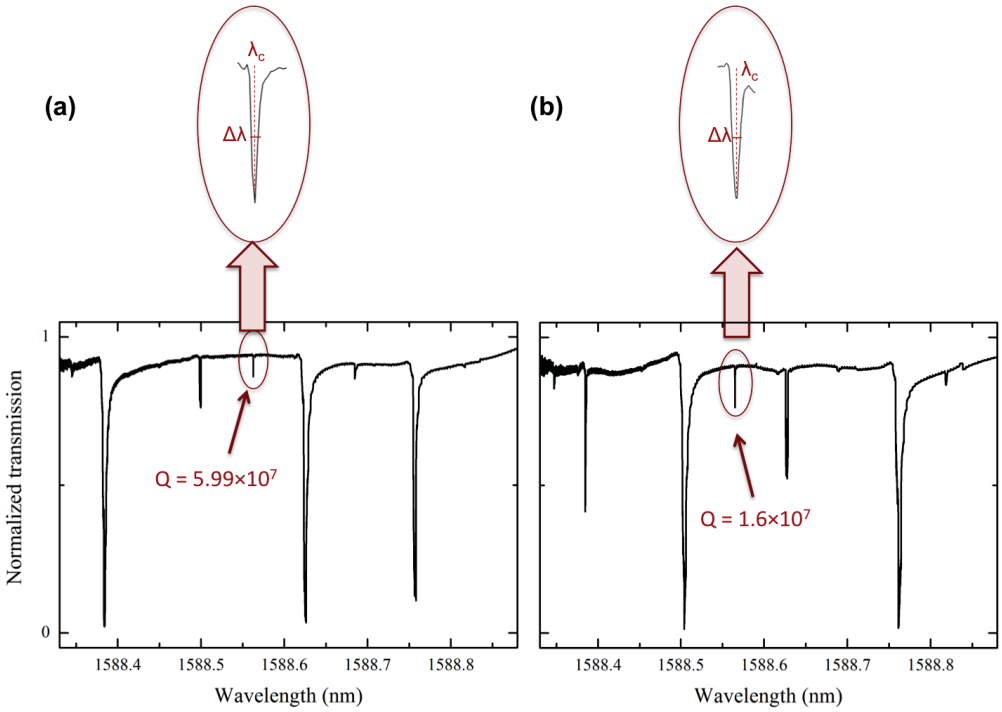

Figure 4.9: **(a)** and **(b)** Normalized transmission at different wavelengths for two different SNAP devices. The spectra show very narrow transmission resonances. Figures (a) and (b) demonstrate the repeatability of quality factors on the order of 10^7.

Silica resonators, such as optical microspheres and fused silica resonators, have quality factors as high as 10^{10} recorded in laboratory conditions [63, 64], the quality factor of ($\sim 10^5$) is considered a good silica resonator, while ($\sim 10^7$) is an ultra high Q-factor.

4.4 Thermal effects

One of the physical processes which produces nonlinear responses in the transmission spectra is the thermal effect. Due to the low optical losses and high quality factor of fused silica microresonators based on WGMs, the field localization V_{eff} (mode volume) of these devices can be as small as $\sim 1000\lambda^3$. The small mode volume of these cavities make them sensitive to thermal nonlinearities [65]. Power lost through absorption inside of the cavity increases and it leads to higher increases of temperature; because the smaller surface area thermal radiation reduces [66]. Therefore, cavity heating cannot be ignored. As a first result, cavity heating causes a hysteric wavelength response of microcavities (as shown in Figure 4.10).

When the laser pumps wavelength (see Figure 4.10(a)) inside a cavity (see Figure 4.10(b)), generally, in the absence of thermal effects, the normalized spectrum shows a drop in the transmission at a resonance wavelength. When the cavity shows a thermal response, due to thermally induced changes of the resonant wavelengths, the normalized transmission spectrum of the cavity changes (see Figure 4.10(c)-blue line).

The dynamical behaviour of a microcavity system was analysed by T. Carmon *et al.*

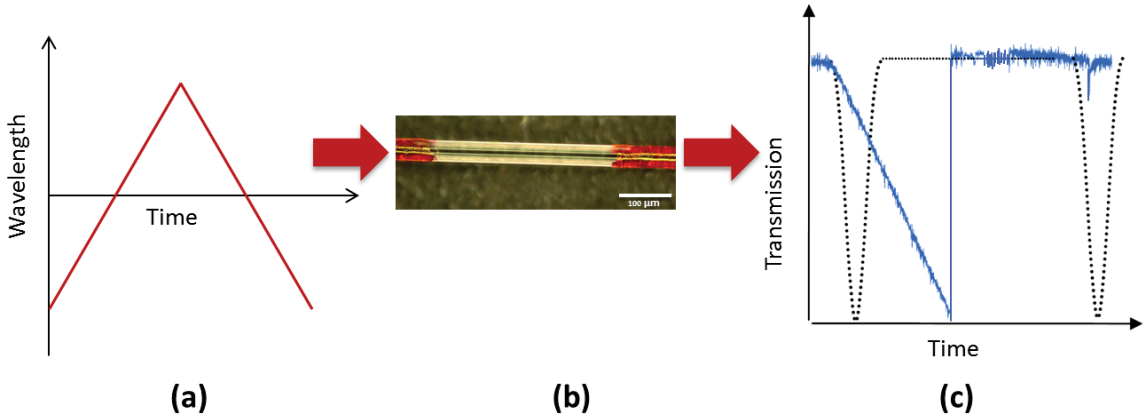

Figure 4.10: Thermal behavior of a cavity. **(a)** A scan of pump wavelength sent to a cavity. **(b)** A microscopic image of a cavity. **(c)** Normalized transmission spectrum of a cavity without the thermal effect (dotted line) and with the thermal effect (blue line). Here, transmission is a function of time.

[67]. The resonant wavelength (λ_r) as a function of temperature for a cavity with refractive index of n_0 is calculated as

$$\lambda_r(\Delta T) \cong \lambda_0[1 + (\varepsilon + \frac{dn}{dT}/n_0)\Delta T] \tag{4.11}$$

where ΔT is the temperature difference between the ambient cavity and the mode volume, λ_0 is the resonant wavelength of the cold cavity, ε is the relative thermal expansion coefficient in units of $1/(^0C)$, and dn/dT is the coefficient of thermal change of the refractive index (units of $1/^0C$) of the medium of cavity.

To simplify Equation 4.11, for both thermal expansion and the thermal index change, a coefficient of thermal change of the resonant wavelength a is defined as

$$a \equiv \varepsilon + \frac{dn}{dT}/n_0 \tag{4.12}$$

Therefore, Equation 4.11 is simplified to

$$\lambda_r(\Delta T) \equiv \lambda_0(1 + a\Delta T) \tag{4.13}$$

For fused silica with a refractive index of $n_0 = 1.46$, $\varepsilon = 10^{-6}(1/^0C)$ and $\frac{dn}{dT} = 0.8 \times 10^{-5}(1/^0C)$ [68], a is calculated as $6.48 \times 10^{-6}(1/^0C)$.

When the transmission spectrum of a SNAP device shows an asymmetric response to a scan of pump wavelength, it means that the resonant wavelength of the SNAP device depends on temperature. When light is coupled into the SNAP devices, it is absorbed. As a result, because of a combination of the thermal expansion coefficient (ε) and the change of the refractive index with temperature (dn/dT), the resonant wavelength is shifted according to Equation 4.11. In a SNAP device made of silica, the latter mechanism is dominant.

Based on the thermal change of the resonant wavelength, the net heat of the cavity is calculated. From energy conservation, the net heat of the cavity is

$$C_p(\dot{\Delta T})(t) = \dot{q}_{in} - \dot{q}_{out} \tag{4.14}$$

where $\dot{q}_{in}$ is the net heat flow into the cavity and is proportional to the pump power

(I), the optical coupling coefficient (k) and the quality factor of the cavity. $\dot{q}_{out}$ is the net heat leaving the cavity and is proportional to the thermal conductivity between the ambient cavity and the mode $K(J/(s^0C)$, while $C_p(J/^0C)$ is the heat capacity of the cavity. The parameter $\dot{q}_{in}$ was formulated by T. Carmon and *et al.* [67] as

$$\dot{q}_{in} = I_h \frac{1}{[\frac{\lambda_p - \lambda_0(1+a\Delta T)}{\Delta\lambda/2}]^2 + 1} \tag{4.15}$$

where λ_p is the pump wavelength, I_h is the actual power heating the cavity, and $\Delta\lambda$ is the resonance bandwidth. Therefore Equation 4.14 was extended as [67]

$$C_p(\dot{\Delta T})(t) = I_h \frac{1}{[\frac{\lambda_p - \lambda_0(1+a\Delta T)}{\Delta\lambda/2}]^2 + 1} - K\Delta T(t) \tag{4.16}$$

Assuming a linear tend of scanning the pump laser wavelength, it is possible to compute the thermal response of the cavity. Figure 4.11 describes the cavity wavelength response as well.

When the pump wavelength moves toward the cavity resonance, the cavity begins to heat up. Therefore, the resonance wavelength of the cavity shifts away from the pump wavelength and they move together. When the pump wavelength reaches the center of the drifted absorption line, the cavity has maximum absorption and stops increasing the temperature. At this position, the absorption cannot increase more to counterbalance the heat dissipation. Further away from this position, the cavity resonance stops moving forward with the pump wavelength and the resonance is lost

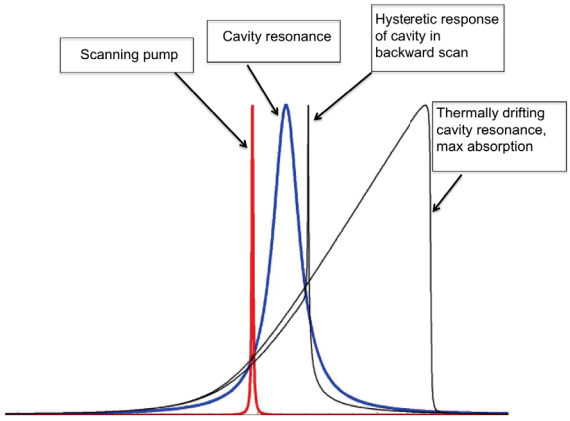

Figure 4.11: Cavity thermal behavior [67].

as its wavelength quickly shifts down and transmission jumps suddenly [69].

During the down wavelength pump scan, the pump wavelength reaches the resonance of the heated cavity again. However, they are propagating in opposite directions. Therefore, the resonance of the cavity turns over with a quick sharp movement with the pump wavelength and causes a hysteric wavelength response [67].

We have been able to observe these phenomena in our SNAP resonators. Figure 4.12 is one of our spectrum results demonstrating significant thermal nonlinear effects.

Figure 4.13 shows a normalized transmission spectrum of a SNAP device. We chose two following dips in this spectrum and zoomed in on them. The first dip is a common resonance mode between a tapered fiber and a SNAP device, while the second dip shows the thermal nonlinear effect due to more electric field inside the SNAP device.

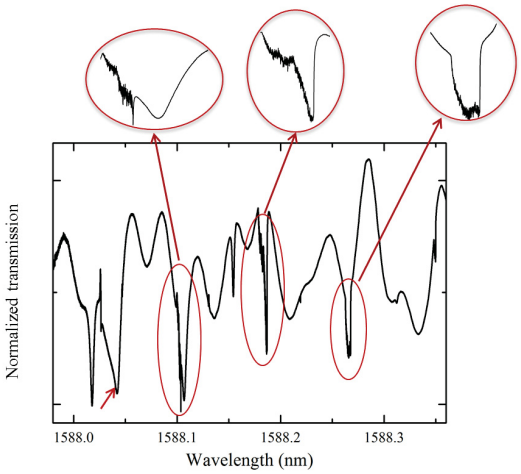

Figure 4.12: Spectrum shows thermal nonlinear behavior.

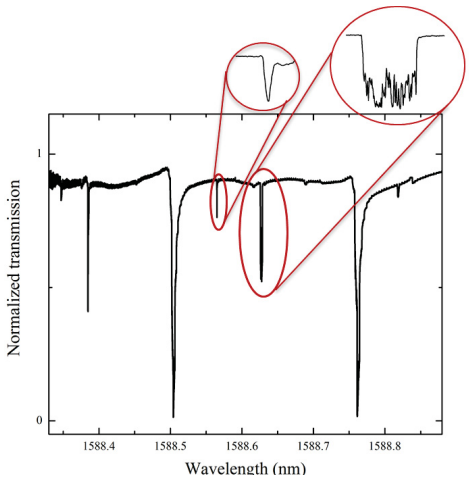

Figure 4.13: Fabricated SNAP devices show significant thermal nonlinear effects.

Chapter 5

Conclusion

Surface nanoscale axial photonics (SNAP) is a new method to produce microscopic optical devices. SNAP resonators are a new generation of whispering gallery mode resonators consisting of an optical fiber with nanoscale variation of its effective radius. The ultra-low surface-limited loss (0.0001 dB/cm) of SNAP resonators leads to extremely good optical modes, with Q-factors (a figure of merit for optical confinement) which can reach values of ten million or higher.

In this thesis, we have first implemented the flame brushing technique to fabricate microfibers (MFs) with different diameters. Microfibers with diameters between $1 - 2\ \mu m$ are used as waveguides with strong evanescent fields. Large diameter microfibers $20 - 80\ \mu m$ are used to make SNAP resonators.

We have introduced a new low cost fabrication method to make SNAP devices. We have characterized the fabricated SNAP devices using the strong evanescent field

from a tapered microfiber. For the characterization of SNAP devices, we designed and built a set-up providing maximum control over the position of the SNAP device and the tapered fiber.

We have estimated the spatial extent of the formed resonator by measuring transmission spectra at different positions along the microfiber. We deduced a spatial extent of 450 μm for one particular SNAP device using this method.

The transmission spectroscopy results show that SNAPs fabricated with a hydrogen-oxygen torch have the potential to host very low loss resonant modes (quality factor up to the order of 10^7), with some resonances demonstrating significant thermal non-linear effects.

For future prospects, we plan to improve our characterization set-up by installing a Fabry-Pérot interferometer in the system to monitor the wavelength of the laser and to more accurately measure transmission spectra. This would allow us to measure the radius variation of our SNAPs. Also, as we collect more quantitative data, we expect to find relationships between the different radius of a SNAP device and its quality factor, the speed of the torch when it passes below the fiber in the second step of making a SNAP device with the different radius or quality factor, and the time-dependence of the second step of producing SNAP device. More theoretical and numerical modelling of SNAP devices is also in our future plans. Moreover, we plan to investigate the changes in resonant wavelength when applying stress to the SNAP device to use it as a turning mechanism. Finally, we would like to make a

cantilever from a SNAP resonator and measure the transmission through the tapered fiber coupled to the SNAP device to learn more about the optomechanical coupling in such devices.

Appendix A

Recipes for fabricating tapered fibers with different diameter

This appendix details recipes to fabricate tapered fibers with different diameters. We set a constant value for some of the parameters (see Table A.1) for all different diameters of tapered fibers. The diameter of a standard single mode fiber with core and cladding is 125 μm.

Table A.1: Uniform parameters for fabrication a tapered fiber

Pulling speed (mm/s): 0.05	Torch speed (mm/s): 13
Torch Y base position (mm): 35.80	Center position (mm): 0
Initial hot zone length (mm): 9	X sweeping speed (mm/s): 2
Minimum torch amplitude (mm): 0.5	Center variation (mm): 1/2

Table A.2 shows the detail of recipes for fabricating a tapered fiber with a diameter between 20 μm to 95 μm. For a tapered fiber with a diameter of 20 μm, pulling

Table A.2: Recipes for fabricating microfibers with diameters between 20 μm to 95 μm

Diameter (μm)	**Pulling duration** (s)				**time to pull** (s)
	$6-8$ (mm)	8 (mm)	$5-10$ (mm)	9 (mm)	
20	61	174	157	114	509
25	61	169	147	110	490
30	61	164	137	104	469
35	56	159	127	104	449
40	46	159	110	97	415
45	41	159	102	89	394
50	36	154	92	84	369
55	21	149	87	79	339
60	21	139	77	69	309
65	21	109	72	64	269
70	21	94	69	65	252
75	21	75	67	55	221
80	21	61	62	51	198
85	21	59	57	49	189
90	21	44	54	42	164
95	11	49	48	43	154

starts at 6 mm. After 61 s, it reaches to 8 mm. It will stay at 8 mm for duration of 174 s. In the next step, pulling will change from 5 mm to 10 mm for 157 s and will remain constant at 9 mm for 114 s. The total time of this process will be 509 s.

The "hot zone length" parameter is defined for different diameters in Table A.3.

Table A.3: The"hot zone length" parameter for different diameters of tapered fibers

D (μm)	**Hot zone length** (mm)
20	[t0:61](4+2/61*t);[t62:236]8;[t237:394](5+5/61*(t-236)];[t395:504]9;
25	[t0:61](4+2/61*t);[t62:231]8;[t232:379](5+5/61*(t-231)];[t380:490]9;
30	[t0:61](4+2/61*t);[t62:226]8;[t227:364](5+5/61*(t-226)];[t365:469]9;
35	[t0:56](4+2/56*t);[t57:216]8;[t217:344](5+5/56*(t-216)];[t345:449]9;
40	[t0:46](4+2/46*t);[t47:206]8;[t207:317](5+5/46*(t-206)];[t318:415]9;
45	[t0:41](4+2/41*t);[t42:201]8;[t202:304](5+5/41*(t-201)];[t305:394]9;
50	[t0:36](4+2/36*t);[t37:191]8;[t192:284](5+5/36*(t-191)];[t285:369]9;
55	[t0:21](4+2/21*t);[t22:171]8;[t172:259](5+5/21*(t-171)];[t260:339]9;
60	[t0:21](4+2/21*t);[t22:161]8;[t162:239](5+5/21*(t-161)];[t240:309]9;
65	[t0:21](4+2/21*t);[t22:131]8;[t132:204](5+5/21*(t-131)];[t205:269]9;
70	[t0:21](4+2/21*t);[t22:116]8;[t117:186](5+5/21*(t-116)];[t187:252]9;
75	[t0:21](4+2/21*t);[t22:97]8;[t98:165](5+5/21*(t-97)];[t166:221]9;
80	[t0:21](4+2/21*t);[t22:83]8;[t84:146](5+5/21*(t-83)];[t147:198]9;
85	[t0:21](4+2/21*t);[t22:81]8;[t82:139](5+5/21*(t-81)];[t140:189]9;
90	[t0:21](4+2/21*t);[t22:66]4;[t67:121](5+5/21*(t-66)];[t122:164]9;
95	[t0:11](6+2/11*t);[t12:61]8;[t62:110](5+5/11*(t-61)];[t111:154]9;

Appendix B

Data processing

As we explained in chapter 4, during the processing of our data we used four python scripts. In this appendix, we report details of these scripts by order of usage. Scripts were written by Dr. Pablo Bianucci.

B.1 make-tc-cal.py

```
#! /usr/bin/python


import sys

import numpy

import pickle


# This script creates a calibration file for our telecom laser diode.
```

```
# It requires a thermistor reading (in KOhm) and the value of the diode current
# when the external modulation is zero volts.


def makecal (filename, temp, I0):
"""Creates a calibration file for the telecom laser diode.
   Arguments:
     'ofile': Output file where to put the calibration.
     'temp': Thermistor reading (in KOhm).
     'I0': Laser current (in mA) when the external modulation is set to zero volts
# Necessary numbers.
# Laser voltage-to-current constant, in mA/V
a = 50
# Wavelength at 50.05 mA according to the temperature, in nm.
lref = 1595.0 * 1.0 *temp**(-0.0015162)
# Polynomial fitting DL(I) = lambda(I)-lambda(50.01 mA)
p = [7.366e-8, 3.8073e-5, 0.0014342, -0.15861 ]
# Wavelength at the center current.
l0 = lref + float(numpy.polyval (p, (I0 - 50.01)))


# First, create a range of currents
I = numpy.arange(0, 100, 0.1)
# Now compute the corresponding voltage.
```

```
V = (I-I0)/a

# Then, we need an array for the corresponding wavelength difference.

DL = numpy.polyval (p, I)


# Debug, output some files.

#numpy.savetxt('debug.dat', numpy.transpose((V, I, DL)))


# Now fit a 3rd degree polynomial to the arrays we have just computed.

# NOTE: This will be used for both the 'up' and 'down' scans!

coeff = numpy.polyfit (V, DL, 3)


# Make a tuple containing the data and a signature.

cucumber = ('LaserCalib', l0, coeff.tolist(), coeff.tolist())

# Pickle the tuple to a file.

with open (filename, 'w') as fh:

pickle.dump (cucumber, fh)


# Main program starts here.


# Process command line arguments

if len(sys.argv) != 4:

print ("Usage:\n\tmake-tc-cal.py <Center current (mA)> <Thermistor resistance (KOh
```

```
sys.exit(1)


I0 = float(sys.argv[1])

Temp = float(sys.argv[2])

fname = sys.argv[3]


makecal (fname, Temp, I0)


# Test...

#with open (fname, 'r') as file:

#    (sig, l0, cf1, cf2) = pickle.load(file)

#print ("Signature: %s" % sig)

#print ("l0 = %g\n", l0)

#print (cf1)

#

#V = numpy.arange(-10, 10, 0.1)

#L = l0 + numpy.polyval (cf1, V)

#

#numpy.savetxt ('l-test.dat', numpy.transpose((V, L)))
```

B.2 MDO-to-scope.py

```
#! /usr/bin/python


import sys

import numpy


# This script loads a file exported from an MDO4000 oscilloscope and converts

# it into the format extract_scope.py needs to extract a single trace from it.

# The oscilloscope has to save "all channels" in CSV format, with the following

# waveform to signal mapping:

#   CH1: Fiber transmission signal

#   CH2: Function generator scanning signal

#   REF1: Not-coupled reference

#   REF2: Zero-transmission (background) reference


# Process command line arguments.

if len(sys.argv) != 3:

print ("Usage:\n\t\tMDO-to-scope.py <infile> <outfile>\n");

sys.exit(1)

infile = sys.argv[1]

outfile = sys.argv[2]
```

```
# Read the traces.
try:
time, ch1, ch2, ref1, ref2 = numpy.loadtxt (infile, delimiter=',', usecols=(0,1,2,
except:
print ("Error reading the data from %s!\n" % infile)
sys.exit(2)

# Output the traces.
try:
numpy.savetxt (outfile, numpy.transpose((time, ch2, ref2, ref1, ch1)), fmt='%.6g',
# Header if using numpy > 1.7.0
#, header="# Time (s)\tLaser voltage (V)\tZero reference (V)\tIntensity reference
except:
print ("Error writing the data to %s!\n" % outfile)
sys.exit(3)

# Exit with a clear status.
sys.exit(0)
```

B.3 savgol.py

```
# Savitzky-Golay filter, lifted from the SciPy Cookbook.
# http://www.scipy.org/Cookbook/SavitzkyGolay
# Added a small interface to apply filtering to a data file.


import numpy
import sys


def savitzky_golay(data, kernel = 11, order = 4, diff = 0):
    """
        applies a Savitzky-Golay filter
        input parameters:
        - data => data as a 1D numpy array
        - kernel => a positiv integer > 2*order giving the kernel size
        - order => order of the polynomal
- diff => which derivative to return (0 is the data)
        returns smoothed data as a numpy array


        invoke like:
        smoothed = savitzky_golay(<rough>, [kernel = value], [order = value]
    """
```

```
try:
        kernel = abs(int(kernel))
        order = abs(int(order))
except ValueError, msg:
    raise ValueError("kernel and order have to be of type int (floats will be
if kernel % 2 != 1 or kernel < 1:
    raise TypeError("kernel size must be a positive odd number, was: %d" % ker
if kernel < order + 2:
    raise TypeError("kernel is to small for the polynomals\nshould be > order


# a second order polynomal has 3 coefficients
order_range = range(order+1)
half_window = (kernel -1) // 2
b = numpy.mat([[k**i for i in order_range] for k in range(-half_window, half_w
# since we don't want the derivative, else choose [1] or [2], respectively
m = numpy.linalg.pinv(b).A[diff]
window_size = len(m)
half_window = (window_size-1) // 2


# precompute the offset values for better performance
offsets = range(-half_window, half_window+1)
offset_data = zip(offsets, m)
```

```
smooth_data = list()


# temporary data, extended with a mirror image to the left and right
firstval=data[0]
lastval=data[len(data)-1]
#left extension: f(x0-x) = f(x0)-(f(x)-f(x0)) = 2f(x0)-f(x)
#right extension: f(xl+x) = f(xl)+(f(xl)-f(xl-x)) = 2f(xl)-f(xl-x)
leftpad=numpy.zeros(half_window)+2*firstval
rightpad=numpy.zeros(half_window)+2*lastval
leftchunk=data[1:1+half_window]
leftpad=leftpad-leftchunk[::-1]
rightchunk=data[len(data)-half_window-1:len(data)-1]
rightpad=rightpad-rightchunk[::-1]
data = numpy.concatenate((leftpad, data))
data = numpy.concatenate((data, rightpad))


for i in range(half_window, len(data) - half_window):
        value = 0.0
        for offset, weight in offset_data:
            value += weight * data[i + offset]
        smooth_data.append(value)
```

```
    return numpy.array(smooth_data)


def main():

if len(sys.argv) < 2:

print "Error! I need a filename!\n"

sys.exit(0)


infile = sys.argv[1]

allcols = numpy.loadtxt (infile)

x = allcols[:,0]

y = allcols[:,1]

sy = savitzky_golay (y, kernel=57, order=5, diff=0)

numpy.savetxt ("smooth.dat", numpy.column_stack((x,sy)))

sys.exit(0)


if __name__ == "__main__":

    main()
```

B.4 extraxt-scope.py

```
#! /usr/bin/python
```

```
# This script loads and process the data that is captured from an oscilloscope
# saved as a CSV or tab-separated file.

# The input file consists of columns, the first one being time (that applies to
# all sets) and the others voltage signals. The different signals, in order,
# are: Laser voltage [1], Zero reference [2], Intensity reference [3],
# data scans [4-...]

# FIXME: It would be nice to skip the CSV intermediate step, and get the
# information directly from the .SHT file, including names for the data columns.

# Version 0.1, 17/Aug/2009
#       * Initial version
# Version 1.0, 31/Aug/2009
# * Finished the wavelength calibration routine.
# * Added checking the number of columns in the file.
# * Now the CSV file can be read directly (instead of preprocessing it
#   with csvtool)!
# Version 1.1, 24/Feb/2010
# * Added the option to choose between CSV or regular whitespace.
# * Fixed the mismatch between the voltage sign and the voltage
#   difference actually applied to the laser cavity piezo.
```

```
#   That error caused the wavelength axis to be inverted around the
#   center!
# Version 2.0, 06/May/2010
# * Now requires an external laser wavelength calibration file, so
#   different diode modules can be accomodated.
#   The proper files are created by the 'wavecal.py' program. They
#   consist of a pickled tuple containing the following objects:
# - A list of polynomial fitting coefficients for the
#   up scanning of the laser voltage (starting with the largest
#   degree).
# - A list of polynomial fitting coefficients for the
#   down scanning of the laser voltage (idem).
# - A string equal to 'LaserCalib' as a signature.
# * Added a header to the output files.
# Version 2.1, 04/Apr/2014
# * Changed the input format to be "time trace_1_V ... trace_n_V".
# Version 2.11, 08/May/2014
# * Added the option to send the data to the standard output.
# * Improved the handling of the background reference to avoid NaNs.


# Import this in order to use a nicer printing to stderr.
from __future__ import print_function
```

```
# Import modules.

from numpy import *

from optparse import OptionParser

from savgol import *


import sys

import pickle



def convert_to_wavelength (l0, calibfname, V):

# Smooth the data to estimate the positions of the global maximum

# and minimum.

print ("\tReading laser calibration data from %s..." % calibfname, file=sys.stderr

try:

calibfile = open (calibfname, 'r')

except IOError:

print ("Error when reading laser calibration data! Aborting!", file=sys.stderr)

sys.exit(2)

(sig, lambda0, polyup, polydown) = pickle.load(calibfile)

calibfile.close()

if sig != "LaserCalib":
```

```
print ("Wrong calibration file format! Did you choose the right file?", file=sys.s
sys.exit(3)
# Use the center wavelength in the calibration file unless l0 is not zero.
if (l0 != 0):
lambda0 = l0


print ("\tFinding maximum and minimum...", file=sys.stderr)
sV = savitzky_golay (V, kernel=255, order=7, diff=0)
xmin = argmax (sV)
xmax = argmin (sV)
step1 = min (xmin, xmax)
step2 = max (xmin, xmax)
print ("\t\tMinimum found at %d, maximum at %d." % (step1, step2), file=sys.stderr
N = len(V)
part1 = []
part3 = []


# Fit the first third (0 to step1).
if step1 > 1:
coeff1 = polyfit (arange(0,step1), V[0:step1], 1)
part1 = polyval (coeff1, arange(0,step1))
if (coeff1[0] > 0):
```

```
#print "Part 1 up!"

part1 = polyval (polyup, part1) + lambda0

else:

#print "Part 1 down!"

part1 = polyval (polydown, part1) + lambda0


# Fit the second third (step1 to step2).

coeff2 = polyfit (arange(step1,step2), V[step1:step2], 1)

part2 = polyval (coeff2, arange(step1,step2))

if (coeff2[0] > 0):

#print "Part 2 up!"

part2 = polyval (polyup, part2) + lambda0

else:

#print "Part 2 down!"

part2 = polyval (polydown, part2) + lambda0


# Fit the third third (step2 to N-1).

if step2 < N-2:

coeff3 = polyfit (arange(step2,N), V[step2:N], 1)

part3 = polyval (coeff3, arange(step2,N))

if (coeff3[0] > 0):

#print "Part 3 up!"
```

```
part3 = polyval (polyup, part3) + lambda0

else:

#print "Part 3 down!"

part3 = polyval (polydown, part3) + lambda0


V2 = hstack([part1,part2,part3])


return (V2, step1, step2)


def main():

# Command line parsing..

parser = OptionParser(usage="Usage: %prog <input data file> <laser calibration dat

parser.add_option("-i", "--initial", type="int", dest="init",

                  help="initial trace to process", default=1, metavar="n")

parser.add_option("-f", "--final", type="int", dest="last",

                  help="final trace to process (0 for all)", default=0, metavar="n

parser.add_option("-r", "--rootname", dest="rootname", default="out-",

help="root name for the output files [default='out-']",

metavar="ROOT")

parser.add_option("-x", "--extension", dest="extension", default="dat",

help="extension to use for the output files [default='dat']",

metavar="EXT")
```

```
parser.add_option("-l", "--lcenter", dest="l0", default="0",
help="force the center wavelength (in nm)")
parser.add_option("-w", "--whole", action="store_false", dest="slice",
default=True, help="don't slice the data to a single ramp")
parser.add_option("-c", "--csv", action="store_true", dest="csv",
default=False, help="read the input file as CSV")
parser.add_option("-s", "--skip", type="int", dest="skr",
help="skip the first n rows from the input data", default=1, metavar="n")

(options, args) = parser.parse_args()

if len(args) != 2:
parser.error ("wrong number of arguments")

if options.last < options.init and options.last != 0:
parser.error ("the final trace cannot be smaller than the initial one")

infile = args[0]
calibfname = args[1]
lambda0 = eval(options.l0)
init = options.init
last = options.last
```

```
slice = options.slice

if options.csv:

delim = ","

else:

delim = None

skr = options.skr


# Find out the number of traces in the file...

# FIXME: What happens if the file is not readable?

with open (infile, 'r') as fh:

fh.readline() # Read the first line and discard.

items = fh.readline().split(delim) # Read and split the second line.


N_col = len(items) - 4 # Converts columns to traces!


# Check the sanity of the last trace option.

if last > N_col or last == 0:

last = N_col


# Convert the traces to columns.

init_col = init + 4

last_col = last + 4
```

```
print ("Processing traces %d (column %d) to %d (column %d)." % (init, init_col, la

# Read the calibration data (traces 1 to 3).
print ("Reading calibration data...", file=sys.stderr)
t, ref_V, raw_bg, ref_I = loadtxt (infile, delimiter=delim, usecols=(0,1,2,3), unp

# Interpolate a linear polynomial for the background.
bgfit = polyfit (t, raw_bg, 0)
ref_bg = polyval (bgfit, t)

# Remove the background from the intensity reference.
ref_I -= ref_bg

# Get the wavelength from the voltage.
print ("Converting to wavelength...", file=sys.stderr)
(wavel, step1, step2) = convert_to_wavelength (lambda0, calibfname, ref_V)

# Process each column.
allcols = loadtxt (infile, delimiter=delim, usecols=(range(init_col-1, last_col, 1
for i in range(0, last-init+1):
print ("Processing trace %d..." % (init+i), file=sys.stderr)
if (last-init+1 == 1):
```

```
data = allcols

else:

data = allcols[:,i]

data -= ref_bg

data /= ref_I

# Remove some non-sensical data (due to noise)

data = where(data >= 0, data, 0)

if slice == True: # NOTE: This is less efficient, but simpler!

outdata = column_stack ((wavel[step1:step2], data[step1:step2]))

else:

outdata = column_stack ((wavel, data))

# Save (or print to standard output) the data.

if options.rootname == "STDOUT":

print ("# Wavelength (nm)\tNormalized intensity", file=sys.stdout)

savetxt(sys.stdout, outdata, fmt="%12.10g")

else:

outname = "%s%d.%s" % (options.rootname, init+i, options.extension)

try:

outfile = open(outname, 'w')

outfile.write("# Wavelength (nm)\tNormalized intensity\n")

savetxt(outfile, outdata, fmt="%12.10g")

except IOError:
```

```
print ("Error writing file %s!\n" % outname, file=sys.stderr)
finally:
outfile.close()


if __name__ == "__main__":
    main()
```

Bibliography

[1] M. Sumetsky, *Localization of light in an optical fiber with nanoscale radius variation*, The European Conference on Lasers and Electro-Optics. Optical Society of America (2011).

[2] M. Sumetsky and J. M. Fini, *Surface nanoscale axial photonics*, Opt. Express. **19** 27, 26470-26485 (2011).

[3] M. Sumetsky and Y. Dulashko, *SNAP: Fabrication of long coupled microresonator chains with sub-angstrom precision*, Opt. Express **20** (25), 27896 (2012).

[4] M. Sumetsky, D. J. DiGiovanni, Y. Dulashko, X. Liu,E. M. Monberg, and T. F. Taunay, *Photo-induced SNAP: fabrication, trimming and tuning of microresonator chains*, Opt. Express **20**, 10684 (2012).

[5] M. Sumetsky, *Delay of light in an optical bottle resonator with nanoscale radius variation: dispersionless, broadband, and low loss* Phys. Rev. Lett. **111**, 163901 Published 17 October (2013).

[6] D. K. Mynbaev, L. L. Scheiner, *Fiber-Optic Communications Technology*, Prentice Hall, New York (2001).

[7] A. Katzir, *Lasers and Optical Fibers in Medicine*, Academic Press city (1993).

[8] G. P. Agrawal, *Applications of nonlinear fiber optics*, Academic Press (2001).

[9] E. Udd, *Fiber Optic Sensors: An Introduction for Engineers and Scientists*, J. Wiley and Sons, New York (1990).

[10] D. Marcuse, J. Stone, *Fiber-Coupled Short Fabry-Perot Resonators*, Journal Lightwave Technology **7**, 869876 (1989).

[11] M. J. Digonnet and C. J. Gaeta, *Theoretical analysis of optical fiber laser amplifiers and oscillators*, Applied Optics **24** 3, 333-342 (1985).

[12] W. D. Heacox, P. Connes, *Optical fibers in astronomical instruments*, The Astron Astrophys Rev. **3**, 169-199 (1992).

[13] L. Tong and M. Sumetsky, *Subwavelength and nanometer diameter optical fiber*, Springer Berlin Heidelberg (2010).

[14] J. Hecht, *City of light: the story of fiber optics*, Oxford university press (2004).

[15] Christopher C. Davis, *Lasers and Electro-optics*, Cambridge University Press (2014).

[16] Safa O. Kasap, *Optoelectronics and Photonics: Principles and Practices*, Prentice Hall (1999).

[17] Fedor Mitschke, *Fiber Optics: Physics and Technology*, Springer (2010).

[18] H. Bach and N. Neuroth(Editor), *The properties of optical glass*, Springer verlag (1998).

[19] J. Heebner, R. Grover, T. Ibrahim, T. A. Ibrahim, *Optical Microresonators: Theory, Fabrication, and Applications*, Springer Science and Business Media (2008).

[20] Kerry J. Vahala, *Optical microcavities*, Nature **424**, 839-846 (2013).

[21] Physics.aps.org.

[22] http://www.nanowerk.com/news/newsid=17259.php.

[23] J. Hu, *Ultra-sensitive chemical vapor detection using micro-cavity photothermal spectroscopy*, Optics Express, **18**, 22174-22186 (2010).

[24] A. Yariv, *Optical Electronics*, Saunders College Publishing, Philadelphia (1991).

[25] M. Sumetsky, *Theory of SNAP devices: basic equations and comparison with the experiment*, Opt. Express **20** (20), 22537-22554 (2012).

[26] M., Sumetsky, K. Abedin, D. J. DiGiovanni, Y. Dulashko, J. M. Fini, and E. Monberg, *Coupled high Q-factor surface nanoscale axial photonics (SNAP) microresonators*, Opt. letters **37** 6, 990-992 (2012).

[27] M. Sumetsky, *Progress in the Surface Nanoscale Axial Photonics (SNAP)*, Transparent Optical Networks (ICTON), 2012 14th International Conference on. IEEE (2012).

[28] M. L. Rabeh, A. S. Samra, and M. Abouheaf, *Evanescent Wave Coupling Between Optical Fiber and Planar Optical Waveguide*, Radio Science Conference, 2006. NRSC 2006. Proceedings of the Twenty Third National. IEEE (2006).

[29] I. Bronstein, K. Semendjajew, G. Musiol, and H. Muhlig, *Taschenbuch der Mathematik*, Harri Deutsch, Frankfurt a.M. (2001).

[30] A. W. Snyder and J. D. Love, *Optical waveguide theory*, London, Chapman and Hall (1983).

[31] M. Sumetsky, *Nanophotonics of optical fibers*, Nanophotonics, **2**, Issue 5-6 (2013).

[32] David J. Griffiths, *Introduction to Quantum Mechanics (2nd Edition)*, Person Education Limited (2004).

[33] M. Sumetsky, *Whispering-gallery-bottle microcavities: the three-dimensional etalon*, Opt. letters **29**, 8-10 (2004).

[34] M. Sumetsky, *Localization of light in optical fibers: Cylinder, conical and bottle microresonators*, Transparent Optical Networks (ICTON), 2011 13th International Conference on. IEEE (2011).

[35] M. Sumetsky, *Mode localization and the Q-factor of a cylindrical microresonator*, Opt. letters **35** 14, 2385-2387 (2010).

[36] M. Sumetsky, *Localization of light on a cone: theoretical evidence and experimental demonstration for an optical fiber*, Opt. letters **36** 2, 145-147 (2011).

[37] *On the Production, Properties, and some suggested Uses of the Finest Threads*, Proc. Phys. Soc. London **9** 8 (1887).

[38] *High-Resolution fibre optics using sub-micron multiple fibres*, Nature **184**, 881-883 (1959).

[39] P. Bianucci, X. Wang, J. G. C. Veinot, and A. Meldrum, *Silicon nanocrystals on bottle resonators: Mode structure, loss mechanisms and emission dynamics*, Opt. Express **18** 8, 8466-8481 (2010).

[40] L. S. Lim, S. W. Harun, H. Arof and H. Ahmad, *Fabrication and applications of microfiber*, Selected topics on optical fiber technology, InTech (2012).

[41] L. Ding, B. Cherif, S. Ducci, G. Leo, and Ivan Favero, *Ultralow loss single-mode silica tapers manufactured by a microheater*, Appl. Opt. **49**, 2441-2445 (2010).

[42] J. M. Ward, A. Maimaiti, Vu H. Le and S. Nic Chormaic *Contributed review: Optical micro- nanofiber pulling rig*, Rev. Sci. Instrum **85**, 111501 (2014).

[43] A. Felipe, G. Espndola, H. J. Kalinowski, Jos A. S. Lima, and A. S. Paterno, *Stepwise fabrication of arbitrary fiber optic tapers*, Opt. Express **20** 18, 19893-19904 (2012).

[44] R. Garcia-Fernandez, W. Alt, F. Bruse, C.Dan, K. Karapetyan, O. Rehband, A. Stiebeiner, U. Wiedemann, D. Meschede, A. Rauschenbeutel *Optical nanofibers and spectroscopy*, Applied Phy. **105**, 1, 3-15 (2011).

[45] G. Brambilla, F. Xu, X. Feng, *Fabrication of optical fibre nanowires and their optical and mechanical characterisation*, Electron. Lett. **42**, 517 (2006).

[46] F. Warken, A. Rauschenbeutel, and T. Bartholomäus, *Fiber pulling profits from precise positioning*, Photonics Spectra **42**, 73 (2008).

[47] R. Kuranea and Y. Nohata, *A new water-absorbing polysaccharide from alcaligenes latus*, Bioscience, Biotechnology, and Biochemistry **58** 2, 235-238 (1994).

[48] S. Pricking and H. Giessen, *Tapering fibers with complex shape*, Opt. Express **18** 4, 3426-3437 (2010).

[49] J. M. Ward, D. G. OShea, B. J. Shortt, M. J. Morrissey, K. Deasy, and S. Nic Chormaic, *Heat-and-pull rig for fiber taper fabrication*, Rev. Sci. Instrum. **77**, 083105 (2006).

[50] T. E. Dimmick, G. Kakarantzas, T. A. Birks, and P. St. J. Russell, *Carbon dioxide laser fabrication of fused-fiber couplers and tapers*, Appl. Opt. **38** 33, 6845-6848 (1999).

[51] L. Shi, X. Chen, H. Liu, Y. Chen, Z. Ye, W. Liao, and Y. Xia, *Fabrication of submicron-diameter silica fibers using electric strip heater*, Opt. Express **14** 12, 5055-5060 (2006).

[52] A. Q. Tool, L. W. Tilton, and J. B. saunders, *Changes caused in the refractivity and density of glass by annealing*, J. Res. Natl. Bur. Std. **38**, 519-526 (1947).

[53] Hans-Rudolf Wenk, Andrei Bulakh, *Minerals: Their Constitution and Origin*, Cambridge University Press, Cambbridge (2004).

[54] J. F. Shackelford, R. H. Doremus *Ceramic and Glass Materials: Structure, Properties and Processing*, Springer Science and Business Media (2008).

[55] http://www.quartzpage.de/about.html.

[56] T. A. Birks and Y. W. Li,*The shape of fiber tapers*, J. Lightwave Technol. **10**, 432 (1992).

[57] M. Sumetsky, D. J. DiGiovanni, Y. Dulashko, X. Liu,E. M. Monberg, and T. F. Taunay, *Robust surface nano axial photonics*, Photonics Conference (PHO), 2011 IEEE. IEEE, (2011).

[58] M. Sumetsky, D. J. DiGiovanni, Y. Dulashko, J. M. Fini, X. Liu, E. M. Monberg, and T. F. Taunay, *Surface nanoscale axial photonics: Robust fabrication of high-quality-factor microresonators*, Optics letters **36** (2011).

[59] S. Bhadra, A. Ghatak, *Guided Wave Optics and Photonic Devices*, CRC Press (2013).

[60] M. Sumetsky and Y. Dulashko, *Radius variation of optical fibers with angstrom accuracy*, Opt. letters **35** 23, 4006-4008 (2010).

[61] A. Boleininger, T. Lake, S. Hami, and C. Vallance, *Whispering gallery modes in standard optical fibres for fibre profiling measurements and sensing of unlabelled chemical species*, Sensors **10** 3, 1765-1781 (2010).

[62] T.A. Birks, J.C. Knight, T.E. Dimmick, *High-resolution measurement of the fiber diameter variations using whispering gallery modes and no optical alignment*, IEEE Photon Technol Lett. **12** 2, 182-183 (2000).

[63] M. L. Gorodetsky, A. A. Savchenkov, V. S. Ilchenko, *Ultimate Q of optical microsphere resonators*, Optics Letters **21**, 453-455 (1996).

[64] L. Collot, V. Lefevreseguin, M. Brune, J. M. Raimond, S. Haroche, *Very high-Q whispering-gallery mode resonances observed on fused silica micro spheres*, Europhysics Letters **23**, 327-334 (1993).

[65] V. B. Braginsky, M. L. Gordetsky and V. S. Ilchenko, *Quality-factor and nonlinear properties of optical whispering-gallery modes*, Phys. Lett. A **137**, 393-397 (1989).

[66] V. S. Ilchenko, and M. L. Gorodetskii, *Thermal nonlinear effects in optical whispering gallery microresonators*, Laser Phys. **2** 6, 1004-1009 (1992).

[67] T.Carmon, L. Yang, and K. Vahala, *Dynamical thermal behaviour and thermal self-stability of microcavities*, Opt. Express **12**, 4742-4750 (2004).

[68] H. Pulker, H. K. Pulker, *Coating on Glass*, Elsevier Science (1999).

[69] T. Carmon, T. Kippenberg, L. Yang, H. Rokhsari, S. Spillane, K. Vahala, *Feedback control of ultra-high-Q microcavities: application to micro-Raman lasers and microparametric oscillators* Opt. Express **13** 9, 3558-3566 (2005).